# MAGMA BODY GEOMETRY AT MOUNT ST. HELENS INFERRED FROM THE STRESS FIELD ASSOCIATED WITH POST-ERUPTIVE EARTHQUAKES

by

**Sally E. Barker**

A thesis submitted in partial fulfillment
of the requirements for the degree of

**Master of Science**

**University of Washington**

**1988**

Approved by _____
(Chairperson of Supervisory Committee)

Program Authorized
to Offer Degree Geophysics Program

Date Aug. 18, 1988

**Master's Thesis**

In presenting this thesis in partial fulfillment for a Master's degree at the University of Washington, I agree that the Library shall make its copies freely available for inspection. I further agree that extensive copying of this thesis is allowable only for scholarly purposes, consistent with "fair use" as prescribed in the U. S. Copyright Law. Any other reproduction for any purpose or by any means shall not be allowed without my written permission.

Signature S Barker

Date August 18th, '88

University of Washington

Abstract

# MAGMA BODY GEOMETRY AT MOUNT ST. HELENS INFERRED FROM THE STRESS FIELD ASSOCIATED WITH POST-ERUPTIVE EARTHQUAKES

by Sally E. Barker

Chairperson of the Supervisory Committee: Professor Stephen D. Malone
Geophysics Program

Earthquakes following the 18-19 May, 1980 and 12-13 June, 1980 explosive eruptions of Mount St. Helens were concentrated at depths below 6 km. The hypocenters of these post-eruptive earthquakes define two seismic lobes separated by an aseismic volume of width 2 km that is located directly beneath the position of the present day cone. The timing and location of the post-eruptive seismicity suggests that the earthquakes occurred in the country rock surrounding a magma body located within the aseismic volume; the withdrawal of magma caused a pressure decrease within the reservoir and the earthquakes occurred as a brittle response to the stress change. Focal mechanism solutions for post-eruptive earthquakes distributed within the seismic lobes are calculated using polarity and amplitude data. Results show that a perturbation from the regional stress field occurs directly beneath the dome between the depths of 7 and 11 km. This anomalous stress field is successfully modeled by a decrease in pressure within a cylindrical magma body located between the seismic lobes and subject to boundary conditions representing the regional stress regime. The position of the anomalous stress field and the distribution of seismicity constrain the magma body geometry to a cylinder of radius 0.9 km, extending from 7 to 11 km and of volume 10 $km^3$. Post-eruptive earthquakes located below 11 km fall on a northeast striking fault that is preferentially aligned with the regional tectonic stress regime to transport magma to the reservoir from greater depths within the crust.

## TABLE OF CONTENTS

## LIST OF FIGURES

## LIST OF FIGURES (Continude)

## LIST OF TABLES

## ACKNOWLEDGEMENTS

Many people have helped me during the time I have spent working towards my Master's degree. Steve Malone provided useful ideas and scientific guidence on many occasions. Tony Qamar and Ken Creager gave helpful reviews of this thesis. Arthur Snoke from V.P.I provided the computer software used to determine the focal mechanism solutions. I also thank my fellow graduate students in the Geophysics and Geology departments for their continuous help and moral support and finally the US-UK Fulbright Commission for their scholarship and encouragement without which I would not have had the opportunity to study in the US.

# CHAPTER I

## ERUPTION SEISMICITY AT MOUNT ST. HELENS

Mount St. Helens volcano began its most recent active phase with the cataclysmic eruption on 18 May 1980. The eruption was initiated by the gravity failure of the bulging North slope, that produced the devastating lateral blast and massive landslide [Christiansen et al., 1981]. Plinian eruptions, ash and pyroclastic flows continued for 9 hours. After 6 hours the eruption entered its most vigorous period and the ash column reached its maximum height. The new pulse of energy coincided with a change in the composition of the magma, visually indicated by a slight change in color of the ash [Malone et al., 1981]. During these initial stages of the eruption, the earthquakes were concentrated between the depths of 3 and 7.5 km and are referred to by Weaver et al., 1987 as the injection swarm. Earthquake signals had high-frequency wave-forms in contrast to the low frequency wave-forms associated with pre-eruption seismicity [Weaver et al., 1981]. The location of events in the injection swarm formed a tight cluster 1 km in radius, located directly below the present vent; earthquakes are interpreted to occur as magma moves upward along a narrow conduit connecting a deeper reservoir with the surface [Scandone and Malone, 1985; Shemeta and Weaver, 1986].

Following the injection swarm seismic activity began to decrease, returning to a much lower level by 20:00 UTC on 19 May 1980, 12 hours after the eruption had ceased. During the post-eruptive phase the seismicity migrated to greater depths in the volcanic system and revealed characteristics of the deeper volcanic system. Between the depths of 7 and 11 km, the hypocenters of the post-eruptive earthquakes define two seismic lobes to the east and west of the present day vent. Within the seismic lobes is an earthquake-free volume that is interpreted to be the location of a magmatic reservoir [Scandone and

Malone, 1985; Shemeta and Weaver, 1986]. The western lobe extends from 11 km to a depth of 20 km in the form of a pipe striking northeast with a plunge of 15 degrees. The injection and post-eruptive swarms ($M_L > 1$) from the May 18, 1980 eruption are illustrated in fig 1.1. Owing to the locations and occurrence times of the post-eruptive earthquakes they have been modeled to occur in the country rock surrounding the magma body as adjustment occurs following a pressure decrease within the reservoir [Scandone and Malone, 1985; Shemeta and Weaver, 1986].

In the depth range 7 to 11 km the spatial distributions of the seismicity that followed the explosive eruptions of Mount St. Helens on 25 May 1980 and 12 June 1980 are very similar to the pattern displayed by the 18-19 May 1980 post-eruptive swarm. Shemeta and Weaver [1986] interpreted the lack of seismic events below 11 km during the later eruptions to indicate that the maximum depth of the magma body was 11 km. Further, to explain the non-circular distribution of earthquakes, they suggested a model for the magma body geometry that is bounded by large controlling faults to the northwest and to the east; however, the focal mechanism solutions calculated in the present study suggest that the earthquakes may have occurred on a system of shorter and discontinuous faults.

The model proposed by Scandone and Malone [1985] and Shemeta and Weaver [1986] aptly explains the temporal and spatial distribution of seismic events between 7 and 11 km that occurred following the explosive eruptions of Mount St. Helens. However, before the model is accepted, it must be tested to determine if the stress field that induced the post-eruptive seismicity, is consistent with that expected from a drop in pressure within a magma body located between the seismic lobes.

The purpose of the present study is to propose and test the model for the magmatic system at Mount St. Helens whereby the withdrawal of magma from a reservoir located

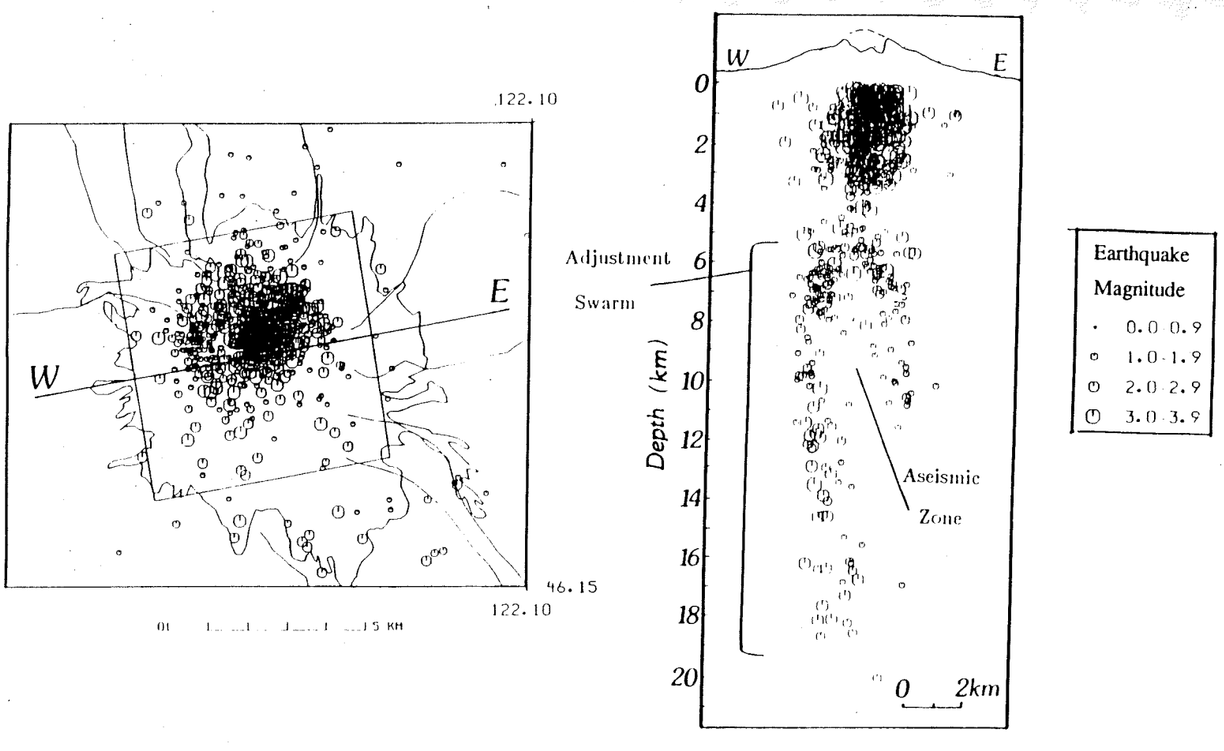


**Figure 1.1** Map and cross-section of Mount St Helens show the locations of the May 18-19, 1980, post-eruptive earthquakes. Between 7-11 km the earthquakes delineate an aseismic volume. Only epicenters within the box are plotted in the cross-section.

between the seismic lobes induced a perturbation in the stress field, inducing the post-eruptive earthquake sequence. Focal mechanism solutions of post-eruptive earthquakes are calculated and the inferred stress field is compared with a theoretical stress field produced by a depressurized cylindrical hole in a infinite elastic region, under boundary conditions equivalent to the regional stress field. The observed focal mechanisms indicate that a perturbation in the regional stress field occurs directly beneath the volcanic edifice between depths of 7 and 11 km . This anomalous field can be successfully modeled in terms of a simple cylindrical magma body extending from 7 to 11 km that undergoes a pressure drop following the withdrawal of magma from a chamber subject to a shear stress regime. Thus, focal mechanism data from post-eruptive earthquakes support the hypothesis that a magma body is located between the depths of 7 and 11 km and that post-eruptive earthquakes occurred in response to a decrease in pressure within this magma body.

# CHAPTER II

# THEORETICAL STRESSES AROUND A CYLINDRICAL HOLE IN AN INFINITE ELASTIC REGION

The stress field produced by a pressure decrease within a cylindrical hole in an infinite elastic region with a shear stress applied in the horizontal plane can be calculated theoretically. If the cylinder is oriented with its long axis lying vertically the geometry represents the model of the magmatic system at Mount St. Helens proposed by Scandone and Malone [1985] and Shemeta and Weaver [1986]. In the following section characteristics of the orientation and magnitude of the stress field surrounding a depressurized cylinder are illustrated as functions of distance from the cylinder, cylinder radius, different stresses applied to the boundaries and pressures within the cylinder.

## Theory

The stress field surrounding a cylindrical hole in an infinite elastic region subject to principal stresses $P_1$ and $P_3$, with internal pressure P in the cylinder, is calculated by superimposing the individual stress fields due to $P_1$, $P_3$ and P. Using general theory of elasticity, the stress field surrounding a cylindrical hole in an infinite elastic region for uniaxial stress $P_1$ can be calculated (Jaeger 1969). The stress functions in polar co-ordinates are of the form[1]:

$$\sigma_r = \frac{1}{2}P_1\left(1 - \frac{a^2}{r^2}\right) + \frac{1}{2}P_1\left(1 - \frac{4a^2}{r^2} + \frac{3a^4}{r^4}\right)\cos 2\theta \quad (1)$$

[1] Although the stress field in this model only varies in 2 dimensions and not with depth, notation is used the is also applicable with the 3-D stress field at Mount St. Helens. Hence maximum and minimum stresses are given subscripts 1 and 3 rather than 1 and 2.

$$\sigma_\theta = \frac{1}{2}P_1\left(1 + \frac{a^2}{r^2}\right) - \frac{1}{2}P_1\left(1 + \frac{3a^4}{r^4}\right)\cos 2\theta \qquad (2)$$

$$\tau_{r\theta} = -\frac{1}{2}P_1\left(1 + \frac{2a^2}{r^2} - \frac{3a^4}{r^4}\right)\sin 2\theta \qquad (3)$$

where a is the radius of the cylinder in the region, and r and θ are the coordinates at which the stress field is evaluated and $P_1$ is applied in the direction of $\theta = 0$. Substitution of $P_3$ for $P_1$ and $(\theta + 90)$ for θ in equations 1 to 3 gives the stress field due to principal stress $P_3$ in a perpendicular direction to $P_1$. The stress field owing to a pressurized cylindrical hole with internal pressure P and with no stresses at infinity is given by:

$$\sigma_r = p\,\frac{a^2}{r^2} \qquad \sigma_\theta = -\,p\,\frac{a^2}{r^2} \qquad (4, 5)$$

The stress field for a pressurized cylindrical hole with principal stresses $P_1$ and $P_3$ is found by superimposing equations 1 with 4, and 2 with 5. [Jaeger, 1969]

$$\sigma_r = \frac{1}{2}(P_1 + P_3) - \frac{a^2}{2r^2}(P_1 + P_3 - 2P) + \frac{1}{2}(P_1 - P_3)\left(1 - \frac{4a^2}{r^2} + \frac{3a^4}{r^4}\right)\cos 2\theta$$

$$\sigma_\theta = \frac{1}{2}(P_1 + P_3) + \frac{a^2}{2r^2}(P_1 + P_3 - 2P) - \frac{1}{2}(P_1 - P_3)\left(1 + \frac{3a^4}{r^4}\right)\cos 2\theta$$

$$\tau_{r\theta} = \frac{1}{2}(P_1 - P_3)\left(1 + \frac{2a^2}{r^2} - \frac{3a^4}{r^4}\right)\sin 2\theta$$

The matrix containing the values of $\sigma_r$, $\sigma_\theta$ and $\tau_{r\theta}$ are diagonalized to obtain the values of the principal stresses $\sigma_1$ and $\sigma_3$ for different values of $\theta$ and r:

$$\begin{pmatrix} \sigma_1 & 0 \\ 0 & \sigma_3 \end{pmatrix} = \begin{pmatrix} \sigma_r & \tau_{r\theta} \\ \tau_{r\theta} & \sigma_\theta \end{pmatrix} \begin{pmatrix} \cos\phi & \sin\phi \\ -\sin\phi & \cos\phi \end{pmatrix}$$

The values of the principal stresses in the rotated coordinate system are given by the eigenvalues $\sigma_1$ and $\sigma_3$; the rotation from the angle $\theta$ is given by the value of $\phi$. The relative positions of the coordinate systems used in the model are illustrated in figure 2.1. To study the characteristics of the stress field around a cylindrical hole in an infinite region theoretical models of the stress distribution are produced by a variety of boundary stresses, $P_1$ and $P_3$, and pressure decrease P, are calculated and illustrated in figures 2.2 and 2.3.

## THE CHARACTERISTICS OF THE STRESS FIELD

### Orientation of the stress field

When a uniform stress field is applied to the boundaries of the region, ($P_1 = P_3$), the stress field around a cylinder at all distances and azimuths shows a radially symmetric pattern. The maximum compressive stress axis, ($\sigma_1$), is aligned tangentially with respect to the boundaries of the cylinder and the minimum compressive stress axis, ($\sigma_3$), is aligned towards the center of the cylinder (fig. 2.3(a)). When a shear stress is applied to the boundaries of the region, ($P_1 \neq P_3$), the stress field is still dominated by the radial pattern at distances close to the boundaries of the cylinder, (fig. 2.3(b)) but with increasing distance from the cylinder the orientation of the axes are dominated by the shear stress applied at the boundaries (fig 2.3(d)). The rate as a function of distance at which the radially dominated stress field rotates to back the shear stress field, depends on both the

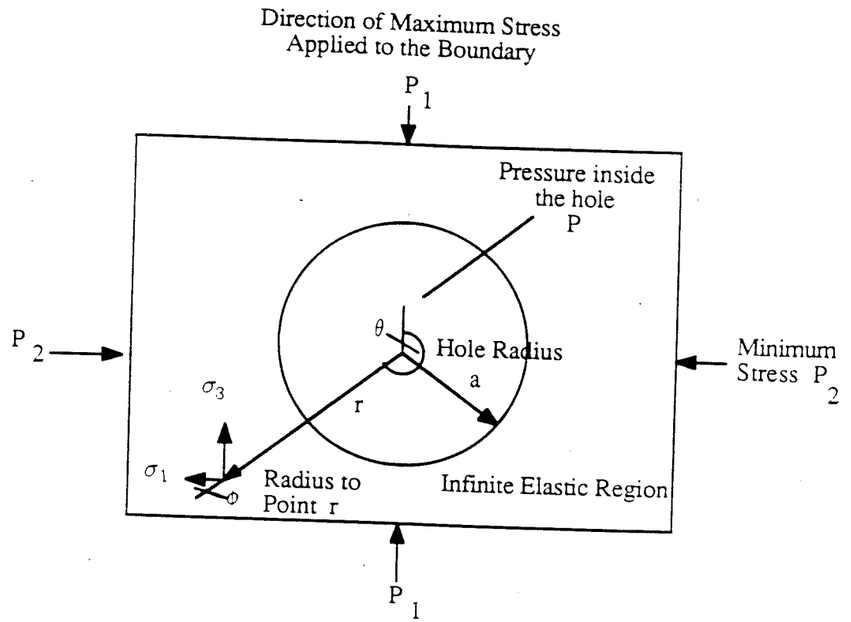


**Figure 2.1** Illustration of the model goemetry.

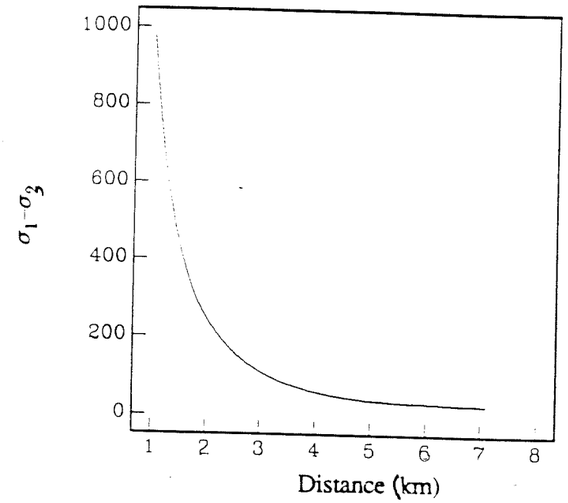


**Figure 2.2** Change in deviatoric stress ($\sigma_1$- $\sigma_3$) with distance from the center of the hole for values of $P_1$=2500, $P_3$=2500, P=2000 (bars) and hole radius 1 km.

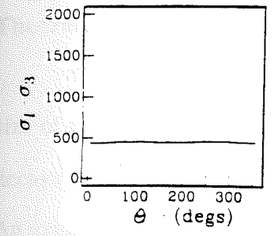


Orientation of $\sigma_1$ Orientation of $\sigma_3$

θ=0 Hole radius=1.0 km

$P_1$ = 2500 bars $P_3$ = 2490 bars P = 2000 bars r=1.5 km

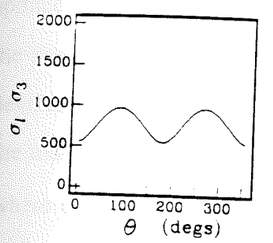


$P_1$ = 2650 bars $P_3$ = 2450 bars P = 2000 bars r=1.2 km

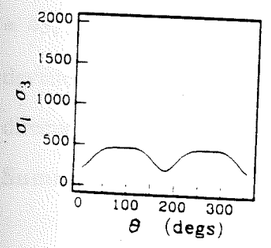


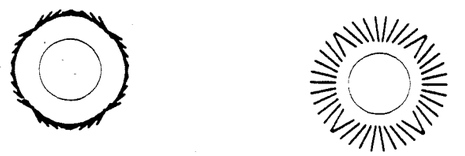

$P_1$ = 2650 bars $P_3$ = 2450 bars P = 2000 bars r=1.8 km

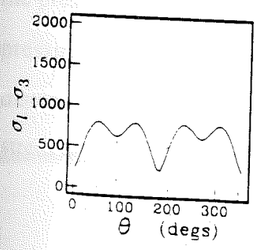


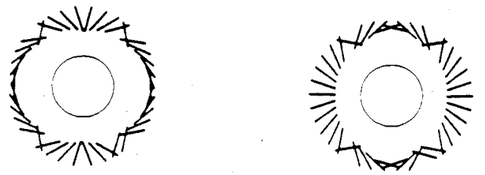

$P_1$ = 2800 bars $P_3$ = 2200 bars P = 2000 bars r=2.2 km

magnitude of the boundary shear stress, ($P_1$ - $P_3$), and the pressure drop within the cylinder.

**Theoretical deviatoric stress field ($\sigma_1$-$\sigma_3$)**

When a uniform applied stress field is applied to the boundaries of the region the size of the deviatoric stress, ($\sigma_1$-$\sigma_3$), is independent of azimuth around the cylinder but decays as $1/r^2$ as the distance from the cylinder r increases (see fig 2.2 and fig 2.3 (a)). An azimuthal dependence of the deviatoric stress is introduced when a shear stress is applied to the boundaries of the region (fig 2.3(b,c,d)). At short distances where the stress field is predominantly caused by the pressure drop within the cylinder, the deviatoric stress has a maximum value at azimuths parallel to the direction of application of the minimum compressive stress ($P_3$) ($\theta$ =90° and $\theta$ = 270°, fig 2.3(c)). In the far-field, where the shear stress field dominates, maximum deviatoric stress values occur in the directions bisecting the direction of the maximum ($P_1$) and minimum ($P_3$) applied stress ($\theta$ = 45, 135, 225, 315° , fig 2.3(d)). For stress fields at intermediate values of r , the deviatoric stress has a maximum value over a broad range of angles that is centered on the direction of $P_3$; a minimum still occurs at azimuths parallel to $P_1$ ( fig 2.3(c)).

**Summary**

At positions close to the cylinder the orientation of the stress field is dominated by the presence of the cylinder, even for very large applied shear stresses and small values of pressure drop. The shear stress component of the stress field becomes larger as the distance from the boundaries of the cylinder increases; the magnitude of the deviatoric stress as a function of $\theta$ becomes less uniform.

# CHAPTER III

# THE DETERMINATION OF THE STRESS FIELD AT MOUNT ST. HELENS

## Data

Seismic records of the post-eruptive earthquakes that occurred on 19 May 1980 and 13 June 1980 are studied in the analysis of the state of stress at Mount St. Helens volcano. Although hundreds of earthquakes were recorded following the explosive eruptions, only a proportion of these events recorded enough high-quality trace data to allow the calculation of focal mechanism solutions. To be of the appropriate quality, the events must have well-constrained locations and several clear P and S phase arrivals. The computer program used to locate the earthquakes [Spong] uses travel time residual statistics and other criteria to rate the locations into quality factors A, B, C and D, with "A" representing the better locations. Events with quality factors A and B are chosen from each of the post-eruptive swarms and a selection is made for a subset of events spatially representative of post-eruptive swarms in the 6 to 20 km[1] depth range. This is the depth range of interest for this study as it includes all of the seismicity surrounding the aseismic volume and also the deeper events. Then the focal mechanism solutions are calculated. The locations of events chosen for this study are illustrated in fig 3.1. All of the events used in the study have high-frequency signals and are classed as type "h" volcanic earthquakes by Malone et al., [1983]. 50 events were analyzed: 39 events from the 19 May 1980 post-eruptive swarm and 11 from the 13 June 1980 swarm. The magnitude range for all the earthquakes in the data set is $0.2 < M_L < 4.0$.

[1]Depths are measured below the mean topographic elevation of the region surrounding Mount St. Helens

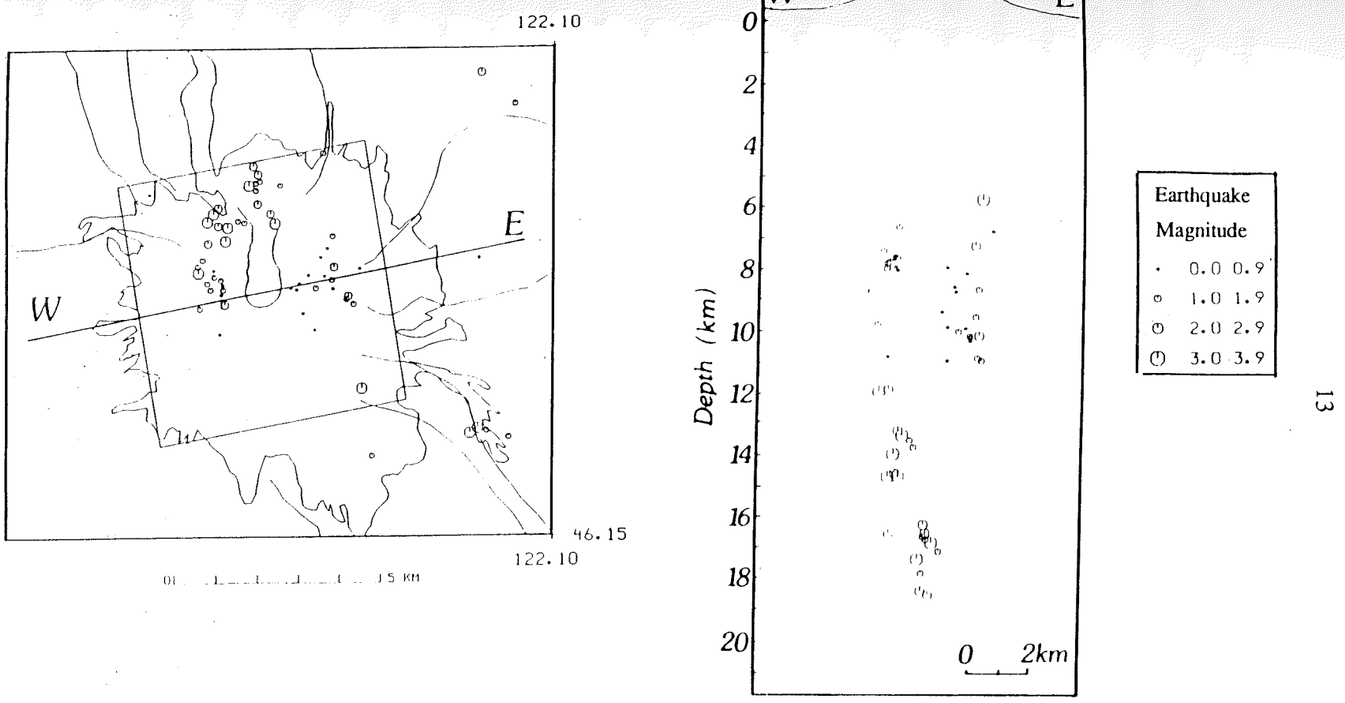


**Figure 3.1** Map and cross-section of Mount St Helens show the locations of the post-cruptive earthquakes selected for the focal mechanism study. Only epicenters within the box are plotted in the cross-section.

In order to make a comparison between the stress field within the volcano and the tectonic stress in the area around the volcanic center, non-volcanic earthquakes locatedaway from the flanks of the volcano and which occurred between 1980 and 1988 were chosen from the University of Washington seismic catalogue . A subset of well-located and evenly distributed events in time and space was selected for analysis. All the epicenters are within a 30 km X 50 km area centered on Mount St. Helens , as illustrated in fig 3.2; the depth and magnitude ranges are comparable with those of the events selected from the post-eruptive swarms.

## FOCAL MECHANISM SOLUTIONS USING AMPLITUDE DATA

Fault plane solutions that are determined using the polarities of the first P wave arrival can give very well-constrained solutions if the data yield good station coverage on the focal sphere, first arrivals are clearly recorded and if the velocity structure is well known. In many cases we find that station coverage is not ideal and that polarity data are sparse; hence, solutions are poorly constrained. For example, despite the dense array of seismic stations at Mount St. Helens, the number of clearly recorded polarities of the first P wave arrival is rarely large enough to determine well-constrained focal mechanism solutions for earthquakes having magnitudes less than $M_L = 3.0$ . If the data set is expanded to include the body-wave amplitude data that were also recorded on the seismogram, better constrained fault plane solutions can be determined.

A method for determining focal mechanism solutions from body-wave amplitude data for hypocentral distances less than 100 km was published by Kisslinger [1980]. The data used for this technique is the ratio of the vertical components of the $S_v$ and P wave amplitudes. It is advantageous to use the ratio of $S_v$ and P wave amplitudes recorded by

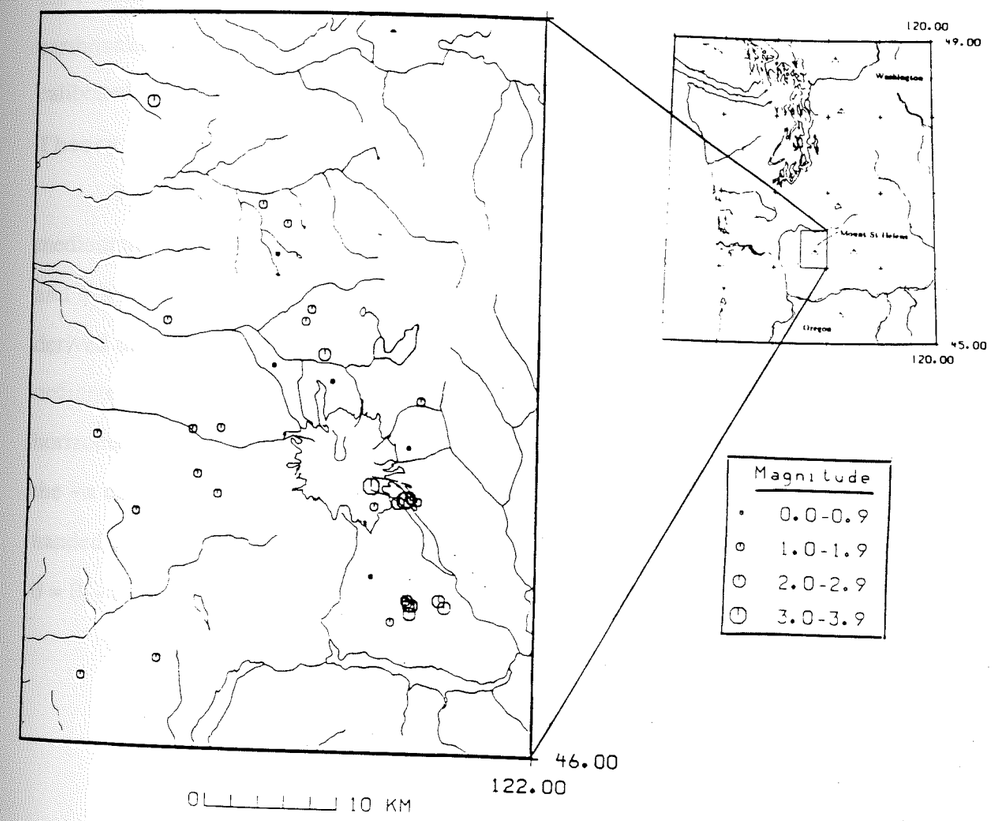


**Figure 3.2** Map view of the 30 x 50 km area that surrounds Mount St. Helens showing the locations of the earthquakes used to determine the regional stress field.

the same seismometer as this ratio ($S_v$/P) does not depend on the recording instrument used. Using this ratio removes any need to make corrections due to varying amplification values on different seismometers and allows the use of uncalibrated seismic stations. For the Mount St. Helens data set the use of the amplitude ratio of ($S_v$/P) is ideal, since the earthquakes are recorded on vertical component instruments, many of which are not calibrated. $\bar{x}$

**Theory**

Vvedenskaya [1956] derived expressions for wave amplitudes in an infinite medium that are generated by a point source shear dislocation. (The radiation patterns for P and S waves are illustrated in fig 3.3.) From Vvedenskaya's equations, Kisslinger has derived the amplitude ratio ($S_v$/P). The fault plane geometry is defined as follows: Co-ordinate system $\bar{x}$, $\bar{y}$, $\bar{z}$ is a reference frame with the surface of the earth ; $\bar{x}$ is horizontal and parallel to the fault strike, dip angle $\delta$ is positive downward to the right from the +x direction; $\bar{z}$ is vertical (positive down); $\bar{y}$ is horizontal and makes a right-handed coordinate system. The take off angle (TAO) $i_h$ is measured upward from $\bar{z}$. $\theta = \theta_s - \theta_f$, where $\theta_s$ is the azimuth to station from the epicenter and $\theta_f$ is the fault strike.

The relationship between $\bar{x}$, $\bar{y}$, $\bar{z}$ and radial distance r and Azimuth $\theta$ is :

$$\bar{x} = r \sin i_h \cos\theta, \quad \bar{y} = r \sin i_h \sin\theta, \quad \bar{z} = r \cos i_h$$

Coordinate system x, y, z is a reference frame with the direction of slip on the fault plane; y is normal to the fault plane, such that angle (y, $\bar{z}$) = $\delta$ ; z is parallel to the direction of slip of the fault block $y < 0$; x makes a right handed coordinate system. The angle (z, $\bar{x}$) = $\lambda$ is measured in the fault plane in a positive clockwise direction about the +y axis. The relationship between the coordinate systems is as follows:

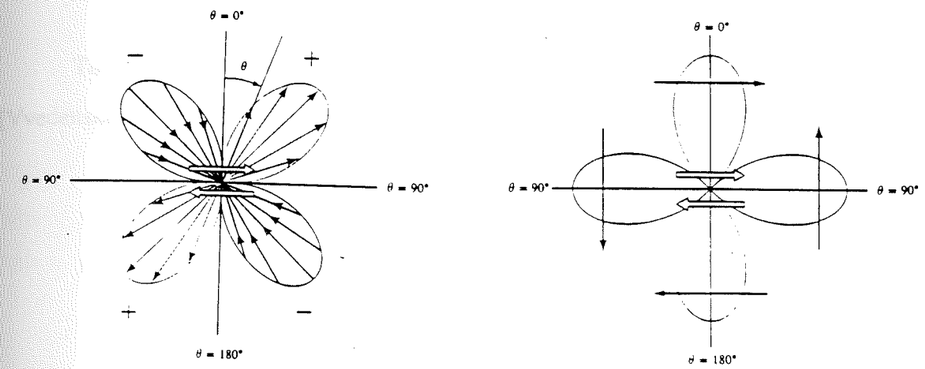


**Figure 3.3** Radiation pattern of P and S waves from a double couple source (from Aki and Richards 1980). The upper illustration is a map view showing the 45° offset of the P and S wave patterns. The lower diagram is a stereographic projection. The symbols + and - represent the polarity of an arrival at a seismic station in that position; "+" compression; "-" dilatation. P is the Pressure axis and T is the Tension axis.

$$x = -\sin\lambda\ \bar{x} + \cos\delta\cos\lambda\ \bar{y} + \cos\lambda\sin\delta\ \bar{z}$$

$$y = -\sin\delta\ \bar{y} + \cos\delta\ \bar{z}$$

$$z = \cos\lambda\ \bar{x} + \sin\lambda\cos\delta\ \bar{y} + \sin\lambda\sin\delta\ \bar{z}$$

The far-field wave amplitudes in an infinite, homogeneous, elastic medium [Vvedenskaya, 1956] are:

$$u_{sv} = \frac{\mu ba\,[-2yz\cos^2 i_h + \bar{z}\,\{z\cos(y,\bar{z}) + y\cos(z,\bar{z})\}]}{\pi\rho V_s^2 r^2 \sqrt{r^2 - y^2}\sin i_h \cos i_h}$$

$$u_p = -\frac{\mu bayz}{\pi\rho V_p^2 r^2 \sqrt{r^2 - y^2}}$$

where $\mu$=shear modulus; b=amount of slip across the dislocation; a=radius of the dislocation: $\rho$=density, $V_p$ and $V_s$ are the P and S wave velocities. The time dependence has been omitted. The ratio of the $S_v$ and P wave amplitudes as they leave the source is given by $(S_v/P)_0$;

$$\left(\frac{S_v}{P}\right)_o = \left(\frac{V_p}{V_s}\right)^3 \cot i_h [2 - \frac{r}{yz\cos i_h}\{y\cos(z,\bar{z}) + z\cos(y,\bar{z})\}]\cot i_h$$

In terms of $\delta,\theta,\lambda$

$$\left(\frac{S_v}{P}\right)_o = \left(\frac{V_p}{V_s}\right)^3 \cot i_h \left(2 - \frac{\{\cot\delta - \tan\delta\}\ L}{D}\right)$$

where

$$L = \sin\lambda\tan i_h \sin\theta + 2\sin\lambda + \csc\delta\cos\lambda\tan i_h\cos\theta$$

and

$$D = \cos\lambda \cos\theta \sin i_h [ -\sin i_h \sin\theta \sec\delta + \cos i_h \csc\delta] +$$
$$\sin\lambda \sin i_h \cos i_h \sin\theta (\cot\delta - \tan\delta) + \sin\lambda (\cos^2 i_h - \sin^2 i_h \sin^2\theta)$$

In the real earth the amplitude ratio ($S_v/P$) must be propagated through the velocity structure to the free surface and then converted to the ratio of the vertical components. The angle of incidence of these components with the free surface is calculated for each take-off angle $i_h$ using ray theory.

$$\left(\frac{S_v}{P}\right)_o = \left(\frac{S_v}{P}\right)_z \text{ x correction factor}$$

$$\text{where correction factor} = \frac{\left(\frac{S_{vo}}{S_{vz}}\right)}{\left(\frac{P_o}{P_z}\right)}$$

Gutenberg [1944] calculated the surface correction factor. Figure 3.4 shows the values of the correction factor with Poissons ratio = 0.25 and assuming plane waves [kisslinger 1981] .

The free-surface effect is easily corrected for $i_h$ between 0-29 and 38-80 degrees. However, the critical angle for $S_v$ to P conversion, is between the angles of 30-37 degrees, and the correction factor changes rapidly even with small changes in incident angle; in the range of 30-37 degrees this factor is very hard to estimate, since any errors in incident angle produce high variations in the correction factor. Thus rays with incident angles of 30-37 degrees are not used in the analysis.

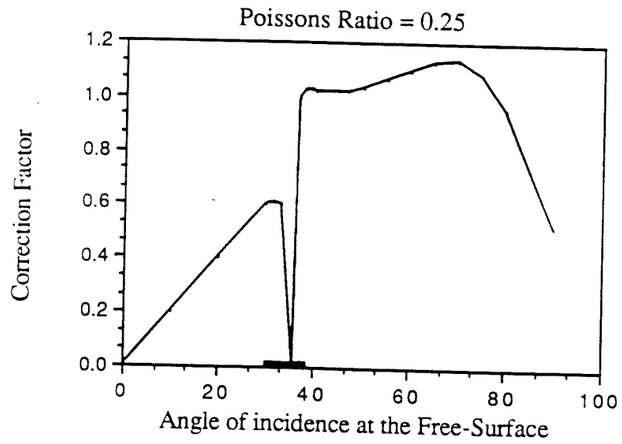


**Figure 3.4** Free-surface correction factor as a function of the angle of incidence at the free surface (from kisslinger 1981). In the shaded region between 30-37° the correction factor varies rapidly. Rays with angles of incidence in this range are not used in the analysis.

**Propagation Effects**

During propagation of the wave from the source to the receiver the amplitude of the P and $S_v$ waves are affected by geometrical spreading of the waves, inelastic attenuation of the material and by partition of energy at internal boundaries. We must correct for any large changes in this ratio due to these propagation effects since it is from the inferred amplitude ratio $(S_v/P)_o$ at the source that the focal mechanism solution is calculated, not from the ratio as measured at the surface.

Geometrical spreading reduces the amplitudes of seismic rays leaving a point source because the wave front expands as it propagates further from the source. The ratio of the P and S wave velocities is approximately constant for all layers of the velocity structure in the Mount St. Helens area [Malone and Pavlis, 1983]. The distances between source and receiver used in this study are less than 50 km and for such short propagation distances the P and $S_v$ waves that arrive at a specific seismic station take approximately the same path. The effect of geometrical spreading on P and S waves is therefore very similar and is assumed to be negligible on the ratio $(S_v/P)$.

The amplitude of the P and $S_v$ waves is also reduced due to the inelasticity of the medium through which the waves are propagating. Inelastic attenuation is described by the quality factor Q . The amplitude at a distance x for a wave with amplitude $A_0$ at the source, frequency $\omega$, wave speed v and quality factor Q is given by:

$$A(x) = A_0 e^{-\omega x/2vQ}$$

The effect of attenuation on the amplitude ratio of $S_v/P$ waves at a distance x where the value of the ratio at the source is $(S_v/P)_0$, with frequencies for the P and S waves $\omega_\alpha$,

$\omega_\beta$ , wave velocities $v_\alpha$ , $v_\beta$ and the quality factors $Q_\alpha$ and $Q_\beta$ can be derived from the above equation and is given by:

$$\left(\frac{S_v}{P}\right)_x = \left(\frac{S_v}{P}\right)_o e^{-\left(\frac{\omega_\beta x}{2v_\beta Q_\beta} - \frac{\omega_\alpha x}{2v_\alpha Q_\alpha}\right)}$$

The values of $Q_\alpha$ and $Q_\beta$ in the Mount St. Helens area are not known. However, studies that measure coda-Q have been undertaken. Using coda-Q values as estimates of shear wave Q values [Aki 1980] the effect of anelastic attenuation for the shear waves can be evaluated. Values of coda-Q in the Mount St. Helens region (for the frequency range of 7-8 Hz) are 112 for a sampling volume of 6 km radius from the volcano [McClurg 1987] and 516 for a sampling volume of radius 50 km [Havskov et al. 1988]. Within the distance range of 0-50 km the amplitude of a shear wave is reduced to $\approx$ 95 % of the amplitude at the source, thus the attenuation effect is small. The effect of attenutation on the amplitude ratio ($S_v$/P) depends on the relative effect of attenutation on the P and $S_v$ waves. The effect of attenuation depends on the different Q values, frequencies and propagation speeds of the P and $S_v$ waves. Values of $Q_\alpha$ for the Mount St. Helens area are not known but $Q_\alpha$ is typically slightly larger than $Q_\beta$ but of the same order of magnitude and the P wave has both a higher frequency and wave velocity than the $S_v$ wave, so $\omega_\beta / v_\beta \approx \omega_\alpha / v_\alpha$. From the above equation it can be seen that the effect of attenuation on the amplitude ratio is smaller than the effect on the shear wave alone and hence is assumed to be negligible for the ratio.

A re-partitioning of energy between the P and S waves can also occur at internal boundaries within a medium. An advantage of using a ratio of the amplitude of ($S_v$/P) is

that for a wide range of velocity contrasts and incident angles the transmission coefficients of P and $S_v$ waves at internal boundaries are close to 1 [kisslinger, 1981]. So the effects of internal boundaries on the amplitude ratio of ($S_v$/P) are small and assumed to be negligible. In summary, all propagation effects are assumed to be negligible. Only the free surface correction is made and I eliminate all observations in which the angle of incidence of the P wave with the free surface is between 30-37 degrees

**Available Computer Software**

Kisslinger [1981] used an iterative least squares inversion routine to find the best fitting focal mechanism solution to amplitude ratio data. He points out that the choice of starting strikes and dips play an important role in finding the correct solution because convergence to the 'wrong' solution might occur if the initial guess is too far off, as many local minima exist within the parameter space due to the non-linearity of the ratio data. In using ratio data alone the fault slip direction cannot be calculated as no sense of motion is recorded in the ratio. Fault strike is often poorly resolved because ($S_v$/P) ratio has a value close to 1 for many azimuth directions and only if a station records a high or low ratio value can the azimuth be highly constrained. A forward-modeling routine for calculating focal mechanism solutions using ratio data was written by Snoke et al [1984]. They overcome the problem of fault slip direction and improve the strike resolution by incorporating polarity data into the calculations. Snoke et al.'s algorithm searches the focal sphere and saves all the fault plane orientations that fit the data to a pre-set standard. Although the forward modeling is more cumbersome than the inverse method, the problem of converging to a local minimum is avoided. In this study of the focal mechanisms solutions at Mount St. Helens, I have followed the procedure outlined by Kisslinger [1981] to prepare the data but have used the algorithm written by Snoke et al.[1984] to make the calculations.

# PROCEDURE USED TO DETERMINE FOCAL MECHANISM SOLUTIONS

For each earthquake, the trace data are examined and the following steps taken:

i) the P wave arrival times are checked and the event is located using SPONG and the St. Helens velocity model [Malone and Pavlis, 1983];

ii) clear impulsive first P wave motion polarities are picked;

iii) $S_V$ and P wave amplitudes are measured where both arrivals are clear;

iv) the angle of incidence at the free surface is calculated for each ray, and the free-surface correction made for each ratio. Ratios from rays with incident angles between 30-37 degrees and refracted arrivals are removed from the data set;

v) for each station, azimuths, take off angles (TOA) at the source, polarities and/or ratios are read into the automatic fitting routine (FOCMEC) which finds the focal mechanism solutions that fit the data to the required standard[2] ;

vi) calculations are made for the mean value of the solutions determined by FOCMEC and for the standard deviation of the mean;

vii) for larger magnitude events without ratio data, the focal mechanism solutions are calculated using an automatic fitting routine called FPFIT that uses polarity data only.

## Picking Polarity and Amplitude Data

Polarity and amplitude data are only used if the data are very clear. When picking the polarity of the P wave first motion I used only unambiguous polarity data. The

[2] Selection criterion are discussed in section FOCMEC

philosophy I have taken with the ratio data is to only measure the ratios if the both P and $S_v$ wave arrivals are impulsive and clearly identifiable.

The value measured for the amplitude of the P and $S_v$ wave is the maximum peak to peak amplitude that occurs in the first 3 half cycles of the arrival. If the $S_v$ wave is at all distinguishable the P wave is usually very clear and its amplitude can usually be measured very precisely. The problems arise when picking the $S_v$ wave arrival. The most common misidentification of the $S_v$ phase occurs when a converted $S_v$-P phase is recorded. The $S_v$ wave and $S_v$-P phase are distinguished by the earlier arrival time and sometimes higher frequency of the converted phase. The $S_v$ travel time residuals are checked so that misidentification of the $S_v$ phase is minimized.

If the timing of the S wave arrival is ambiguous but the S wave package is clear, a maximum estimate of the $S_v$ amplitude can be inferred from a measurement of the maximum amplitude in the S wave package. The value recorded is the largest possible value of $S_v$ amplitude and hence a maximum allowed value of the ratio ($S_v$/P). Later solutions with theoretical ratio values greater than this maximum value are rejected from the set of acceptable solutions. The amplitude is also measured as a maximum or minimum value when either the P or $S_v$ wave is clipped (but not both). Data recorded in this qualitative manner have either lower or higher values of $S_v$/P ratio than ratios determined by direct measurement. Having a wide range of ratio values is very important in the determination of the focal mechanism solutions because for large parts of the focal sphere, the $S_v$/P ratios are close to one and only a small number of take off angles produce ratios which have extreme values. Hence the addition of these qualitative measurements leads to more highly constrained focal mechanism solutions.

## The calculation of the focal mechanism solutions using FOEMCE fitting program (Snoke et al, 1984 )

The program searches the focal sphere and lists all the fault plane solutions that fit the observed data to within the ranges specified by the selection criterion. The following choices are made for each run of the program:

i) the number of allowed polarity errors for a solution to be valid;

ii) an acceptable range for deviations between the observed and calculated amplitude ratio;

iii) the number of ratio errors that are allowed to be outside the range;

iv) the coarseness of the search of the focal sphere.

The program computes the ratio values for the listed stations at all search orientations, then compares theoretical value with the observation. If the solution stands up to the selection criterion controlling the amount of polarity and ratio data error, then the solution is listed along with the theoretical and observed values of the amplitude ratios; otherwise, the solution is rejected. For the stations having qualitative data (max or min values of the amplitude ratio) the theoretical and observed ratio values are compared, and solutions with incompatible values are rejected. The value for the allowable ratio error used in the analysis is 0.1; it represents an estimation of the ratio amplitude measuring error assuming that the correct phase is being measured. Initially the focal sphere is searched every three degrees looking for solutions with no polarity or ratio errors. If more than seven acceptable solutions are found they are checked to see if the solutions fall in the same region of the focal sphere . If the range of acceptable solutions[3] covered a localized

[3] Solution fitting the section criterion

area of the focal sphere, I found that relaxing the constraints and allowing more errors merely enlarged the spread of the solution around the previous mean and did not produce drastically different solutions. If less than seven solutions are determined, the selection criterion are slowly relaxed allowing polarity and ratio errors to increase until 7 acceptable solutions are found.

## LIMITATIONS OF THE METHOD AND VELOCITY MODEL

The validity of the assumptions in the method for determining the focal mechanism solutions and for the velocity model used in the analysis are considered below. The reasonable nature of allowing non-perfect fit between the data and acceptable focal mechanisms solutions is also discussed.

### Limitations of the Method

In the analysis, I looked for the best double-couple solution to explain the data. Although the seismic signals generated by these earthquakes are tectonic in character, it is possible that some of the earthquakes studied have a small non-double-couple component to the focal mechanism solution whereby all the polarity and ratio data will not fit the theoretical values.

### Limitations of the velocity model

The velocity model used for the Mount St. Helens region (Malone and Pavlis, 1983) is a layered 1-D model that is only an approximation to the gross velocity structure of the area; One would expect lateral variations in the velocity structure to occur in the vicinity of the volcanic center (Lees and Crosson, 1988). The unmodeled lateral variations in the velocity structure are the main source of location error. Variations in the location of an event alter the T0A of the ray from the source and change the position of the data points on

the focal sphere. Variations in depth affect the TOA much more than variations in the horizontal direction due to the layering of the velocity structure in the vertical plane. The largest variation occurs when an event is relocated in a velocity layer above or below the layer in which it was originally located. The average depth error in the event locations used in the study is 1.0 km , with a largest error of 1.9 km. To study the effect of location errors on focal mechanism solutions, five earthquakes were selected from the catalogue at ranging depths and magnitudes; they were then relocated 2 km above and below their original locations. Many events were relocated in different velocity layers that provided worst case variations in TOA. Their focal mechanism solutions were then calculated in the manner outlined in the previous section. The range of Pressure and Tension axes determined by FOCEMC is illustrated in the map and the cross-section in figure 3.5. The locations of the earthquakes used are given in table 3.1 and mean axis directions of the P and T axes are given in table 3.2.

Providing that the selection criterion in the FOCMEC routine was relaxed until at least five or six satisfactory solutions were found, (searching at 3 degree intervals), most of the solutions fall in similar areas of the focal sphere even when the hypocenter was relocated by $\pm$ 2 km. I conclude that errors derived from limitations in the velocity structure do not cause a greater variation in the range of focal mechanism solutions than the range of acceptable solutions determined by FOCMEC, assuming the selection criterion in FOCMEC is relaxed until at least 5 or 6 solutions are found.

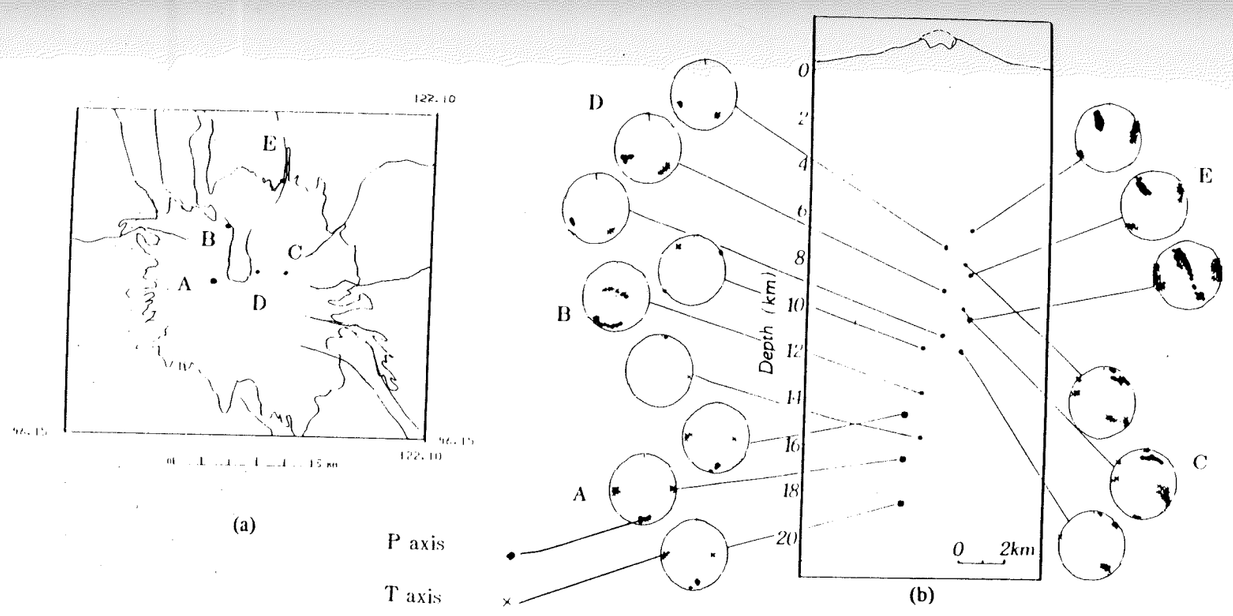


**Figure 3.5** (a) Locations of the earthquakes used in the error analysis. (b) Location and focal mechanisms solutions of earthquakes A, B, C, D, and E before and after relocation ± 2 km. The results are illustrated in terms of the P and T axes on lower hemisphere stereographic projections and are determined using the program Focmec. The data are also listed in tables 3.1 and 3.2.

**Table 3.1** Location data for earthquakes used in the error analysis.

| Event | Date | Time | Latitude | Longitude | Depth | M |
|---|---|---|---|---|---|---|
| A | May 19, 1980 | 0106 | 46.1185°N | 122.1211°W | 17.43 | 2.2 |
| B | May 19, 1980 | 0200 | 46.1286°N | 122.1175°W | 14.44 | 1.7 |
| C | May 19, 1980 | 0752 | 46.1204°N | 122.1007°W | 10.66 | 0.6 |
| D | May 19, 1980 | 0709 | 46.1205°N | 122.1087°W | 9.85 | 0.2 |
| E | May 19, 1980 | 0721 | 46.1372°N | 122.1028°W | 9.07 | 1.5 |

**Table 3.2** Focal Mechanisms Solutions: Events at Depths ± 2 km
Lower hemishpere projections are illustrated in fig 3.5

| Event | Depth | P axis | | T axis | |
|---|---|---|---|---|---|
| | | Strike | Dip | Strike | Dip |
| A | 15.43 | 173 | 14 | 270 | 26 |
| | 17.43 | 164 | 21 | 260 | 14 |
| | 19.43 | 169 | 14 | 260 | 5 |
| B | 12.44 | 55 | 0 | 325 | 21 |
| | 14.44 | 198 | 12 | 341 | 75 |
| | 16.44 | 7 | 6 | 98 | 10 |
| C | 8.66 | 34 | 12 | 129 | 24 |
| | 10.66 | 17 | 17 | 114 | 20 |
| | 12.66 | 43 | 10 | 137 | 20 |
| D | 7.85 | 249 | 24 | 145 | 29 |
| | 9.85 | 245 | 33 | 169 | 23 |
| | 11.85 | 242 | 21 | 143 | 21 |
| E | 7.07 | 327 | 39 | 65 | 10 |
| | 9.07 | 330 | 40 | 238 | 3 |
| | 11.07 | 341 | 48 | 259 | 3 |

# A COMPARISON OF TWO METHODS TO DETERMINE FOCAL MECHANISM SOLUTIONS

## Focmec vs Fpfit. (With and without ratio data)

For the earthquakes with magnitudes larger than $M_L = 3.0$ a large amount of polarity data is recorded, but amplitudes recorded at seismic stations close to the epicenter are so large that most traces have clipped arrivals for both the P and $S_v$ waves. Therefore, the focal mechanisms for the larger earthquakes in the data set are calculated using an automatic fitting program called FPFIT [Reasenberg and Oppenheimer, 1985] that uses polarity data alone.

In order to compare the the quality of solutions found by these two methods, I have selected an earthquake from the Mount St. Helens region with enough polarity data to yield a well-constrained solution, and also with enough ratio data so that a focal mechanism solution can be calculated using FOCMEC.

The focal mechanism solutions were calculated by FPFIT and FOCMEC using all of the available data (runs 1&2). Then to approximate the amount of data available when studying the smaller earthquakes located under the cone of Mount St. Helens, the focal mechanism solutions were calculated using a subset of the data (run 3). Finally a solution is calculated by FPFIT excluding the polarity reading at station FMW [4] (run 4). The results are shown in fig 3.6 as lower hemisphere stereo projections . The data for each run is recorded in table 3.3 and solutions are listed in table 3.4

[4] Polarity reading FMW was controlling the solution and it was noticed that only a small change in the velocity model would cause the take-off angle for a ray going to FMW to be mapped onto the other side of the hemisphere and thus change the solution drastically.

Run 1

Polarity Data

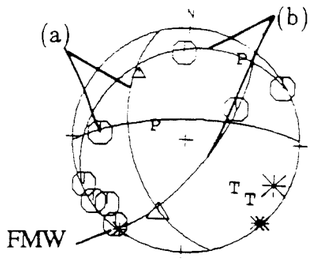


Run 2

Polarity and Ratio Data

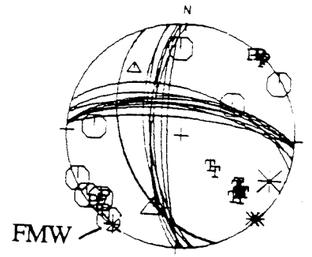


Run 3

Reduced Data set

5 Polarities

6 Ratios

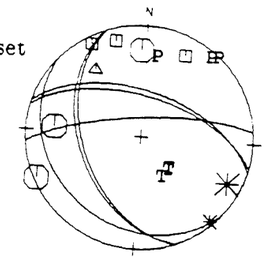


key

- 'C'
- '+'
- 'D'
- '-'
- Ratio

Run 4

13 Polarities

(no FMW)

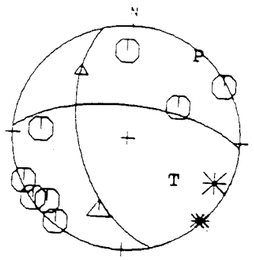


**Figure 3.6** Lower hemisphere projection of the focal mechanism solutions determined in runs 1-4. Solutions to runs 1 and 4 are calculated using polarity data alone, solutions to runs 2 and 3 use both polarity and ratio data. The data used in each run and the solutions are listed in tables 3.3 and 3.4.

**Table 3.3** Polarity and Ratio data for the earthquake used to illustrate the mertis of FOCMEC

| Station | Key* | Data Used in Run 1 | Data Used in Run 2 | Data Used in Run 3 | Data Used in Run 4 |
|---|---|---|---|---|---|
| KOS | d | √ | √ | | √ |
| FMW | c | √ | √ | | |
| LON | d | √ | √ | | √ |
| COW | d | √ | √ | | √ |
| WPW | d | √ | √ | | √ |
| GLK | d | √ | √ | √ | √ |
| SBL | d | √ | √ | | √ |
| SBL | r | | √ | √ | |
| SOS | d | √ | √ | √ | √ |
| SOS | r | | √ | √ | |
| SHW | d | √ | √ | √ | √ |
| ELK | d | √ | √ | | √ |
| RVW | d | √ | √ | | √ |
| CMM | c | √ | √ | √ | √ |
| CMM | r | | √ | √ | |
| CPW | c | √ | √ | | √ |
| APW | c | √ | √ | √ | √ |
| CDF | r | | √ | √ | |
| JUN | r | | √ | √ | |
| FLT | r | | √ | √ | |

* Key : c,d are polarity readings,
r is a ratio reading.

**Table 3.4** Focal mechanism solutions determine when comparing fpfit and focmec.

| Date | Time | Latitude | Longitude | Depth | M |
|---|---|---|---|---|---|
| March 2, 1982 | 0201 | 46.2090°N | 122.1478°W | 11.12 | 1.1 |

| | P axis | | T axis | |
|---|---|---|---|---|
| | Strike | Dip | Strike | Dip |
| Run 1(a) | 31 | 16 | 135 | 40 |
| (b) | 289 | 64 | 133 | 24 |
| Run 2 | 225 | 1 | 135 | 36 |
| Run 3 | 28 | 14 | 144 | 59 |
| Run 4 | 37 | 7 | 133 | 44 |

Using all the polarity data FPFIT finds two quite different solutions: (a) and (b). (b) differs from (a) because solution (b) is controlled by the compressional arrival recorded at station FMW. Solutions determined by FOCMEC for both the full and reduced data sets, run 2 & 3, are very similar to solution (a) in run one. However no comparison can be made with a solution determined using polarity data alone for the smaller data set since FPFIT was unable to determine a solution due to lack of data. Run 4, was a re-run of FPFIT using all the polarity data excluding the polarity data at station FMW; this run produced solution (a) that was determined in run 1.

The earthquake used for this study falls on the St. Helens seismic zone [Weaver et al., 1987] which is a right lateral strike-slip fault running approximately North-South. The "correct" focal mechanism solution for this event is probably similar to the solution selected using the ratio data or solution (a) in run 1, rather than solution (b) in run 1. In summary, the result of this comparison shows that:

i) solutions determined using ratio data in addition to polarity data are very consistent with well-constrained solutions determined using polarity data alone;

ii) when only small amounts of polarity data are available (5 or 6 data points) solutions can be determined that are consistent with those found using many more polarity readings, if ratio data is included in the calculations;

iii) The addition of ratio data decreases the sensitivity of the solution to any one polarity reading, as illustrated by solution (b) and the polarity reading at station FMW.

The focal mechanisms solutions determined using FPFIT and FOCMEC are treated as one data set irrespective of their slightly different methods of calculation.

# RESULTS OF THE ANALYSIS

## Focal Mechanism Solutions of the Post-eruptive and Regional Earthquakes

The results of the focal mechanism studies are most easily illustrated by the orientation of the Pressure (P) axis and the Tension (T) axis. In map view diagrams, a line is drawn in an orientation that represents the azimuth of the axis and the dip of the axis is indicated by the length of the line. A line of 1.5 cm represents an axis lying horizontally, a point represents a vertical axis. In the cross-section diagrams the line is at the angle of dip of the axis and the length of the line decreases as the azimuthal direction of the axis moves out of the plane of the cross-section. The line becomes a point when the axis is perpendicular to the plane of the cross-section. In all the diagrams the width of the line represents the estimated error of the focal mechanism solution. For solutions determined by FOCMEC, the error is estimated to be equal to the standard deviation of the range of acceptable solutions. If the mechanism is determined using polarity data alone the error is assigned a value of 15 degrees. Earthquake location data, mean focal mechanism solutions and lower hemisphere projections of the range of solutions determined for the events used in this study are given in the Appendix. Earthquake epicenters are represented by open circles and the size of the circle is proportional to the magnitude of the event. In map view diagrams the position of Mount St. Helens volcano is represented by the 5000' contour level, which is approximately the same height as the pre 1980 tree line.

### The regional stress field in the area surrounding Mount St Helens.

The focal mechanism solutions of events located off the flanks of the volcano are projected onto a map of the Mount St. Helens area and onto a NW-SE cross-section through the region. (fig 3.7 and fig 3.8). The average orientation of the Pressure axis in

122.00
46.00
122.00
T axis
0 10 KM


122.00
46.00
122.00
P axis
0 10 KM

122.00
122.00
T axis
0 10 KM
46.00
46.00
122.00
122.00
P axis
0 10 KM

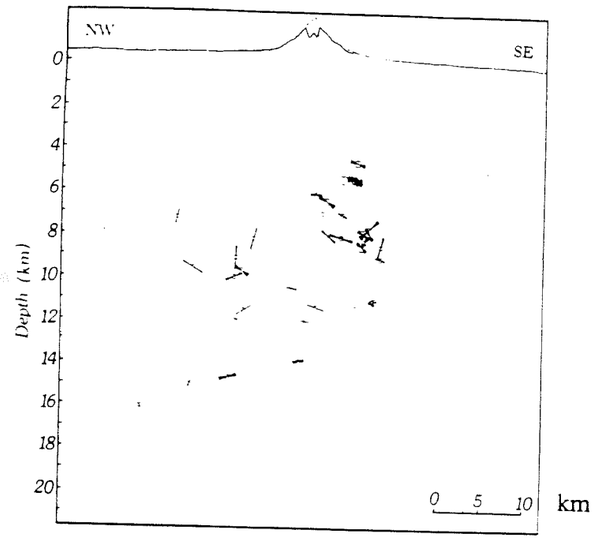
NW
SE
0
2
4
6
8
10
12
14
16
18
20
Depth (km)
0 5 10
km

T axis

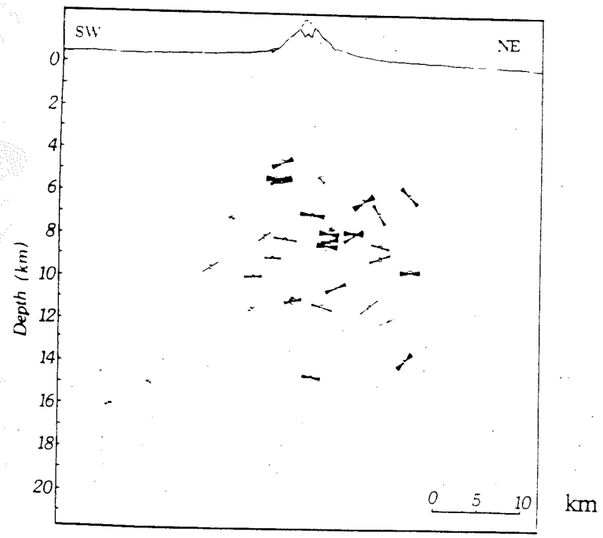
SW
NE
0
2
4
6
8
10
12
14
16
18
20
Depth (km)
0 5 10
km

P axis

Regional Earthquakes

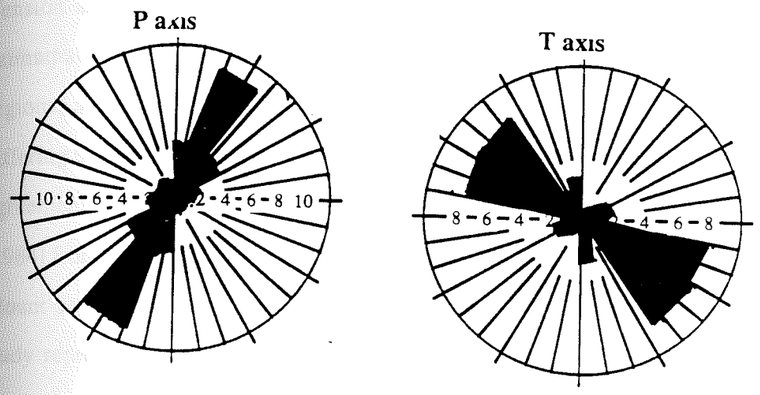


Post-eruptive Earthquakes

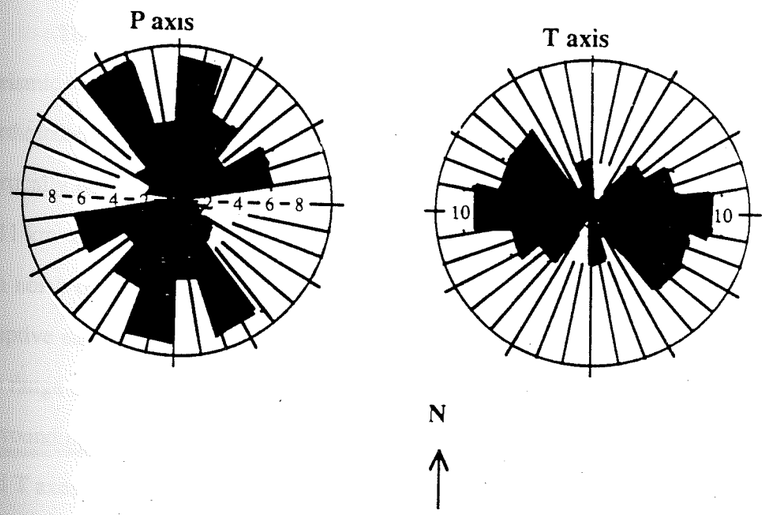


**Figure 3.9** Projection of the azimuthal orientation of the P and T axis for regional and post-eruptive earthquakes.

the Mount St. Helens region is N 40 E dipping at 0-5 degrees to the southwest . The Tension axis is oriented N 60 W and dips to the southeast. Rose diagrams of the azimuthal orientations of the principal axis, fig 3.9, show the uniform orientation of the regional stress field, only a small number of events having focal mechanism solutions differing from the mean. The direction of the principal axes determined in this study are in agreement with the orientations found for Pressure and Tension axes by Grant et al. [1984] from their study of the earthquakes in the Elk Lake sequence located to the North of Mount St. Helens. I shall infer that the orientation of the P and T axes calculated in this study represent the directions of the maximum and minimum compressive stresses in southwest Washington. These directions are in agreement with those inferred by Weaver and Smith [1983] from their study of earthquakes in southwestern Washington .

**Stress regime within the volcanic edifice at Mount St Helens.**

The post-eruptive earthquakes are located on two seismic lobes which surround an aseismic volume [Scandone and Malone 1985]. Locations and magnitudes of post-eruptive earthquakes located below 6 km are illustrated in fig 3.10. The eastern lobe extends almost vertically below 7 km to a depth of 11 km. The western lobe also extends vertically from 6-11 km and then dips to the northeast such that the earthquakes located at 20 km are 2 km north of the present dome. This deeper seismicity includes the largest of the post-eruptive earthquakes. The magnitude of events located at depths greater than 11 km is in the range of $2 < M_L < 4$, in contrast to $0 < M_L < 2$ for the events at more shallow depths surrounding the aseismic volume. Fig 3.13 illustrates in map view the orientation of the P and T axes between the depths of 6-20 km. The orientations of the Pressure and Tension axes determined for the post-eruptive earthquakes are very different from those found for the regional non-volcanic earthquakes. The principal stress components form a circular

pattern centered on the cone-shaped aseismic volume. The T axis is oriented perpendicular to the boundaries of the volume, while the P axis lies tangential to the boundaries. Fig 3.14 shows a cross-sectional view of the P and T axis. The average dip angles of the P and T axes are similar to the dip of the regional stress field. Fig 3.9 is a rose diagram and illustrates both the P and T axis orientations for the post-eruptive earthquakes and the regional earthquakes. For the post-eruptive earthquakes the stress axes are oriented in many different azimuths in contrast to the very uniform NE-SW, NW-SE orientation of the stress field of the P and T axes for the regional earthquakes. The main feature for the post-eruptive earthquakes is the wide range in azimuthal orientations of the principal stress axes despite the very localized area in which the earthquakes occur.

As the average magnitude of events in the depth range 7-11 km is smaller than the magnitude of events located below 11 km and the aseismic volume is only defined on 2 sides up to a depth of 11 km the data set is divided into two groups. Events located above 11 km and events located below 11 km. The change in the character of the seismicity at 11 km is clearly seen in figure 3.10. Figure 3.13 shows the orientation of the P and T axes for the different depth ranges, in map view, and figure 3.14 illustrates the azimuthal variation in rose diagram format. Studying figure 3.13 and comparing figure 3.9 and 3.14 show that the post-eruptive events in the depth range 7-11 km have stress fields that are perturbed from the regional stress field direction, but the deeper and larger magnitude earthquakes have stress fields that are similar to the regional stress field. This suggests that the earthquakes occurring above and below 11 km have a different controlling processes.

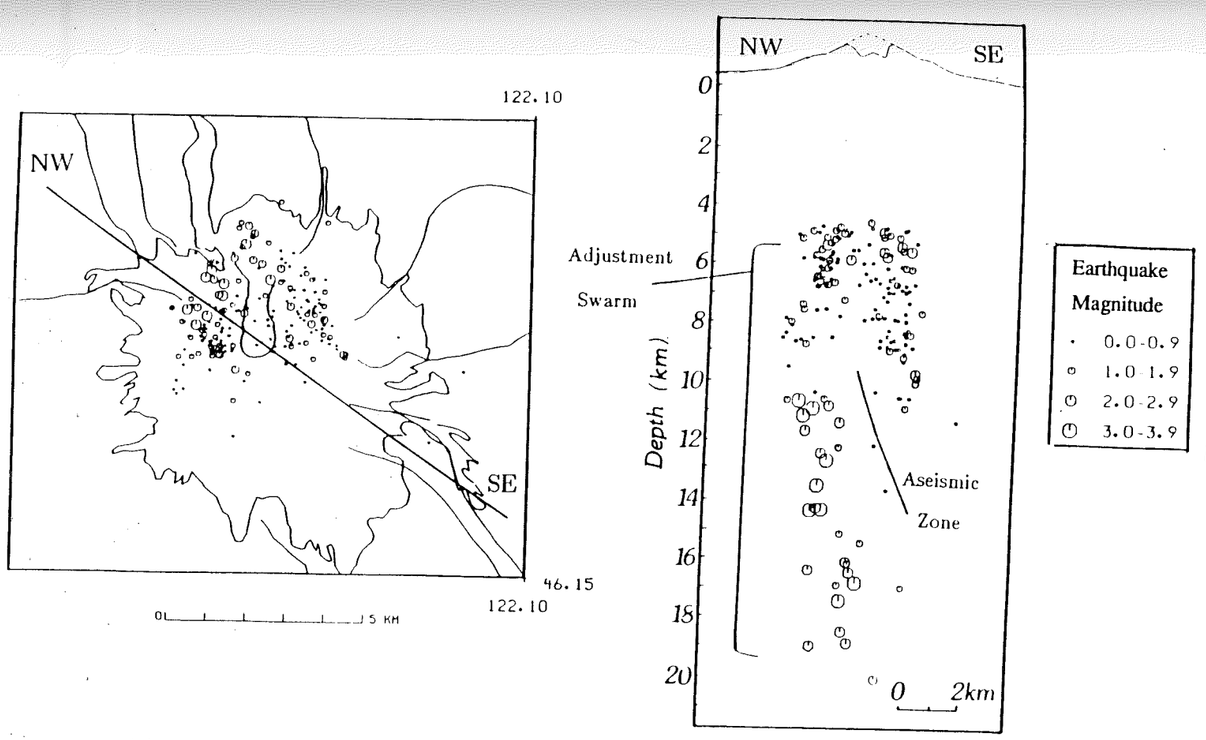


**Figure 3.10** Map and NW-SE cross-section of Mount St. Helens show the locations of the earthquakes from the May 19, 1980 and June 13, 1980 post-eruptive swarms. Note the small size of the earthquakes surrounding the aseismic zone in the depth range 7-11 km and the change in character of the seismicity below 11 km to much larger events.

122.10

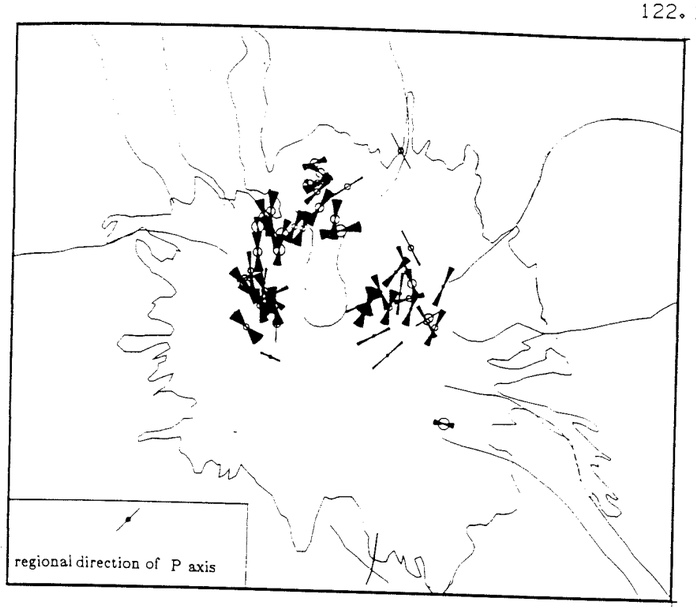


46.15

46.15

122.10

122.10

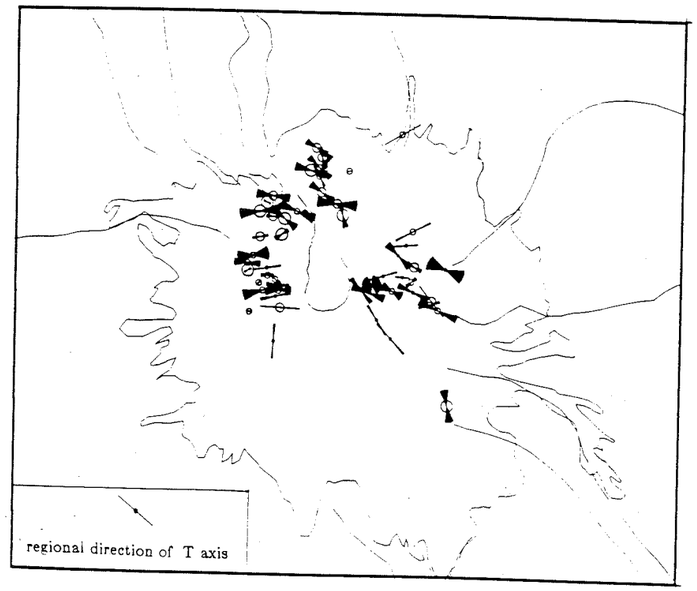


46.15

46.15

122.10

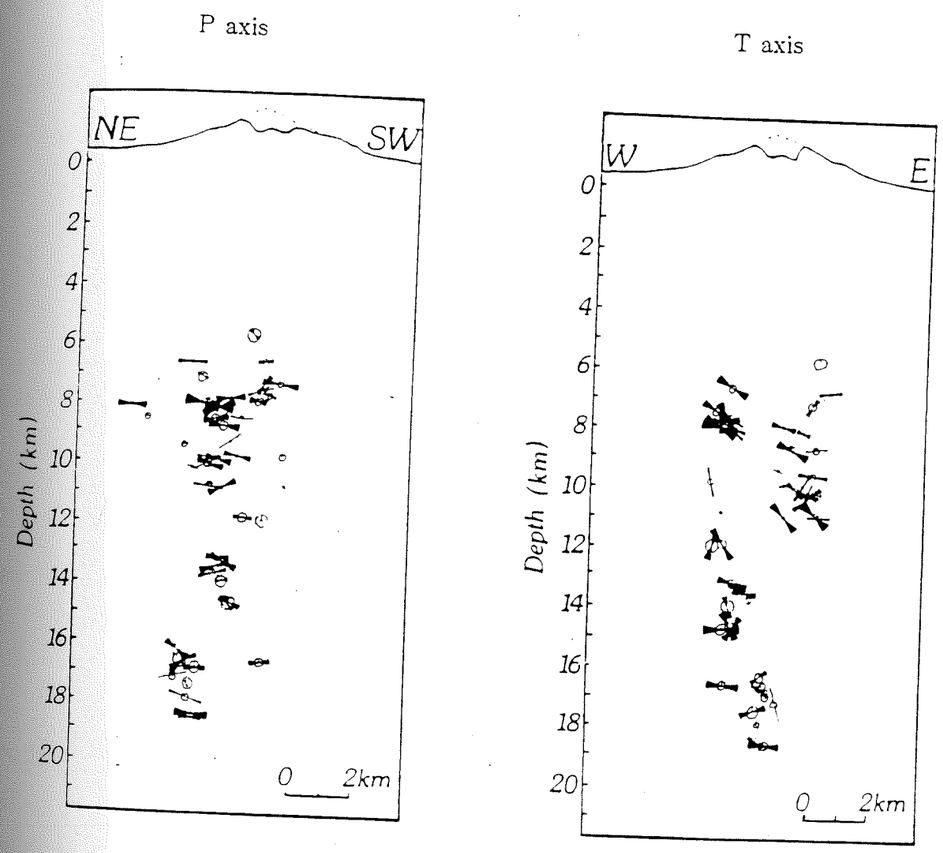


**Figure 3.12** Dip of the P axis projected onto a NE -SW cross-section through Mount St. Helens and dip of the T axis projected onto a E-W cross-section. The length of the axes decrease as the strike of the axis moves out of the plane of the cross-section. The plane of the cross-sections are aligned with the average strike the axes. The dips of the P and T axis for the post-eruptive earthquakes show a similar distribution to the regional stress field (fig. 3.8).

122.10

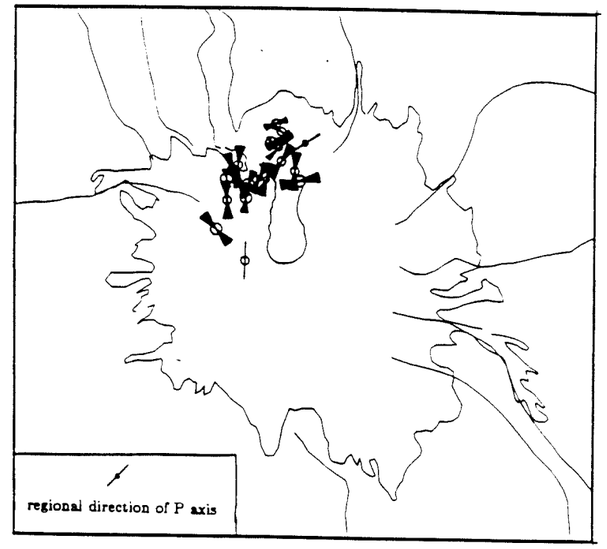


46.14 46.14

122.10

122.10

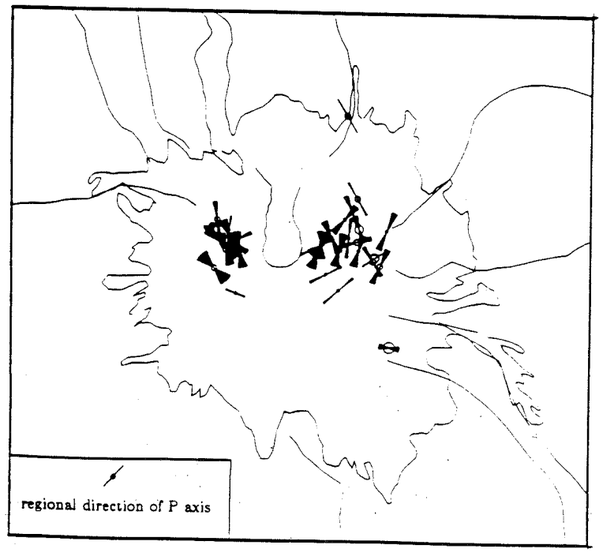


46.14 46.14

122.10

0 5 KM

Post-eruptive Earthquakes Depth range 7-11 km

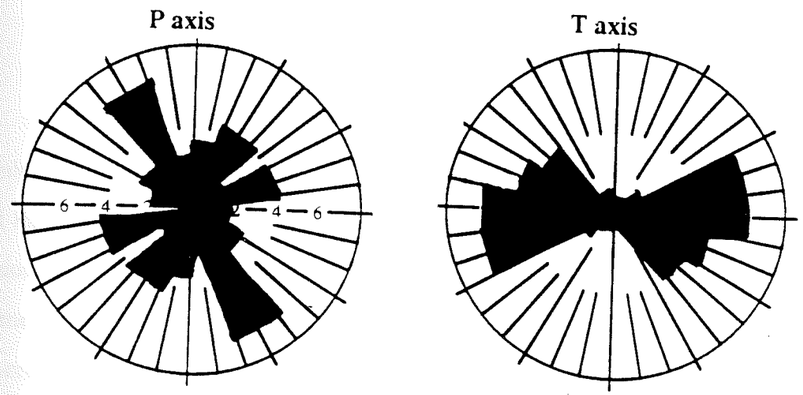


Post-eruptive Earthquakes Depth range 11-20 km

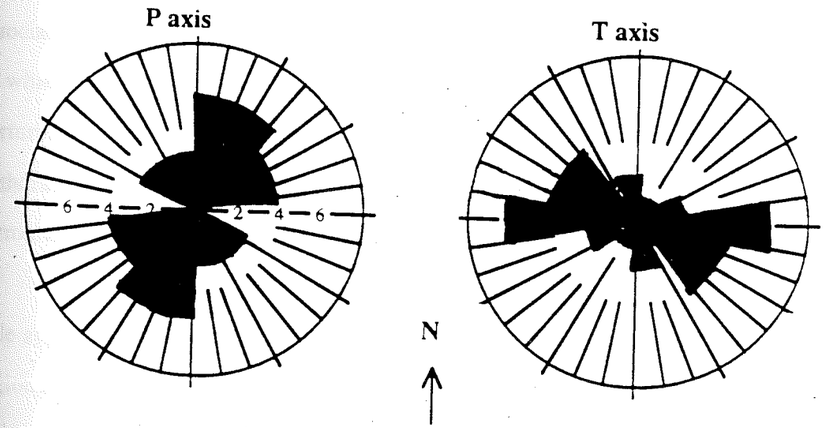


**Figure 3.14** Projection of the azimuthal orientation of the P and T axis for post-eruptive earthquakes divided into events located above and below 11 km. The distribution for the events located below 11 km is similar to the distribution or the regional stress field ( fig. 3.9).

# CHAPTER IV

# MODELING THE ANOMALOUS STRESS FIELD

## Results of a 2-D model

The study of the focal mechanism solutions of post-eruptive earthquakes located directly under the cone of Mount St. Helens reveals a stress regime in the depth range of 7 to 11 km which is quite different from the regional stress field. In this depth range, the location of the two lobes of seismicity form a symmetrical pattern around a central aseismic volume, which is the possible position of a magma body. The stress field associated with post-eruptive earthquakes located below 11 km has a similar orientation to the regional stress field and the character of the seismicity changes to larger earthquakes that are located to only one side of the aseismic zone. This indicates that in contrast to the more shallow earthquakes, regional tectonics control the seismicity below 11 km. The association of the post-eruptive earthquakes with explosive eruptions of Mount St. Helens in which large volumes of material were ejected from the volcano, suggest that the perturbation of the stress field between the depths of 7 and 11 km is caused by the withdrawal of magma from a magmatic reservoir and the earthquakes occur in the rock surrounding the magma body in response to the perturbation in the regional stress field.

This system is modeled in terms of an infinite elastic region with a cylindrical hole at pressure P within it representing the magmatic reservoir. The boundaries of the region are subject to a shear stress equivalent to the regional stress field in the Mount St. Helens area. To test the deflating magma body hypothesis, theoretical values of the stress field around the cylindrical hole are calculated for parameter values suitable for Mount St. Helens. The model predicts the magnitude and orientation of the principal axes in the horizontal plane; the dip is not modeled. However, this is an appropriate model for the

stress field at Mount St. Helens because the most striking difference between the stress fields is the rotation in azimuth of the axes. The inclination of the stress field associated with the post-eruptive earthquakes does not appear to be perturbed. In both stress fields the majority of P and T axes lie in the horizontal plane. The derivation of the equations used in the calculations are shown in Chapter 2, Modeling Theory.

**Modeling Strategy**

Given values of the stresses on the boundaries of the region and the pressure drop within the cylindrical hole, one can calculate the magnitude and orientation of the maximum compressive stress, ($\sigma_1$), and the minimum compressive stress, ($\sigma_3$), around the hole at different radial distances. To model the orientation of the stress field one can make a straight forward comparison between the orientation of the theoretical stress field and the stress field inferred from the study of the focal mechanism solutions of post-eruptive earthquakes. The magnitude of the stresses acting within the volcanic system are not known so direct comparisons of theoretical and observed values cannot be made, but by invoking the following reasoning an estimate for the theoretical breaking stress of the rock can be inferred and compared with values of earthquake stress drop.

For an earthquake to occur, the deviatoric stress ($\sigma_1$- $\sigma_3$) must be larger than the stress needed to break the rock. Since the deviatoric stress produced in the above model decreases with distance from the cylinder as $\frac{1}{r^2}$ (Illustrated in fig 2.2), one can assume that at a distance beyond which no post-eruptive seismicity was induced, the magnitude of the deviatoric stress, is less than the value of the breaking strength of the rocks. At Mount St. Helens the maximum extent of seismicity from a central point is about 2 km, so the value of the theoretical deviatoric stress at this maximum distance is assumed to be the breaking stress of the rock.

**Determining the values of the model parameters.**

The model parameters are the radius of the cylinder, the pressure drop within the cylinder,(P), the maximum and minimum compressive stress,($P_1$,$P_3$), to be applied at the boundaries. The magnitude and orientation of the maximum and minimum compressive stresses,($\sigma_1$, $\sigma_3$), are evaluated at points (r,$\theta$) in the region. The appropriate values for model parameters at Mount St. Helens are discussed below.

The maximum size for a circular hole centered between the seismic lobes can be estimated from the location of post-eruptive seismicity, assuming no earthquakes occur inside the cylinder. In the depth range 7 to 11 km the average distance between the seismic lobes, and hence the inferred maximum diameter of a cylinder is 2.0 km. In actuality, the seismicity may not occur very close to the boundaries of the magma body and a more realistic model may include the simulation of a smaller magma body with a zone between the boundary of the magma body and the seismicity in which plastic deformation of the rocks occurs. During modeling the theoretical stress field is calculated for cylinders with radii of 1 km, 0.75 km and 0.5 km to accommodate the above models.

The focal mechanism study of the region around Mount St. Helens, as shown in Chapter 3, illustrates that the dominant fault movement is right lateral strike-slip motion, as found by other authors [Weaver et al., 1987; Grant et al., 1984]. From this it is inferred that both the maximum ($P_1$) and minimum ($P_3$) compressive stress axes lie in the horizontal plane thereby allowing $P_1$ and $P_2$ to represent the boundary conditions that are applied horizontally in the model. The magnitudes of the principal stresses are not known, but the intermediate principal stress axis lies vertically in the region around Mount St. Helens; thus the magnitude of the vertical stress is equal to the lithostatic overburden. At a depth z, the value of the lithostatic stress is given by :

$$P_2 = \rho\, g\, z$$

where ρ is the density of the rock and g is the acceleration due to gravity and z is depth. At 10 km $P_2 \approx 2.7$ kbars. The magnitudes of $P_1$ and $P_3$ by definition are greater than, and smaller than $P_2$ respectively. Values in the range of 2800-2720 bars for $P_1$, and 2680-2600 bars for $P_2$ are used in the modeling. When a shear stress, $P_1 - P_3$, greater than 200 bars is applied to the region and when using the other estimated parameter values, the circular nature of the stress field is not apparent. As the orientation of the stress field is the feature that is being modeled, results with shear stresses larger than 200 bars (values of $P_1$ =2800, $P_3$ = 2600) are not shown.

No geophysical measurements have been made that allow a direct estimation of the pressure drop within the volcanic system during the eruption, and hence a more basic approach has been used to estimate the pressure drop within the magma body. The fundamental driving force of a volcanic eruption is the buoyancy of the magma. When a volcanic system is opened, as after the landslide at Mount St. Helens on 18 May 1980, magma rises from depth towards the surface, decreasing the pressure within the volcanic system. The rise of magma is caused by a density differential between the magma and the surrounding rock. For short lived eruptions, especially plinian types as seen at Mount St. Helens, it is believed that the rate at which the magma escapes from the chamber is much greater than the rate at which it can be replaced from a deeper source. In the case where no replenishment of magma from a deeper source occurred, the pressure drop ΔP within a body of magma is given by the equation for hydrostatic pressure [Scandone and Malone 1985].

$$\Delta P = (\rho_s - \rho)\, zg$$

where $\rho_s$ is the density of the country rock and

ρ is the density of the magma and z is depth.

In his gravity modeling Williams et al., [1987] estimated a density of 2.7g $cm^{-3}$ for the rocks directly beneath Mount St. Helens, while for extruded magma the density is estimated to be 2.46 g $cm^{-3}$ [Olhoeft et al., 1981]. Using values for the acceleration due to gravity, $g \approx 10^3$ $cm^{-2}$, and depth z=10 km , a pressure drop of $\approx$ 240 bars is produced.

Estimations of the pressure drop within the magma chamber can also be made by calculating the fraction of magma extruded relative to the total volume of magma in the chamber, an equivalent measure of the proportional drop in the pressure of the system. Actual estimates have been made for the volume of tephra extruded from the volcano on 18 May 1980 [Sarna-Wojcicki et al.,1981]. A volume of 0.2 $km^3$ was calculated by summing the of volumes of ash deposited in areas around the volcano; hence this value is a rough estimate of the minimum volume of magmatic material extruded from the volcano. To estimate the size of the magma body, one can measure the size of the aseismic zone, although an independent estimate of the actual volume of fluid within the magma body must be made for the following reason. As mentioned previously, the possibility exists that the seismicity does not occur at the boundaries of the magma body owing to the existence of a plastic zone. The volume of the aseismic zone is approximately 12 $km^3$. Assuming the chamber originally had 7 $km^3$ of fluid within it, and that the pressure values in the chamber were on the order of those for lithostatic pressure, then the drop in pressure within the chamber is estimated at 80 bars, for a volume of 0.2 $km^3$ of magma extruded during the eruption. As the estimate of the volume of tephra extruded from the mountain is inherently a minimum estimate, the pressure drop of 80 bars represents an estimate of the minimum pressure drop within the system. In addition, the inferred volume of the magma body and the estimated volume of erupted products are only known very roughly, which render only an order of magnitude value for the estimate of the minimum pressure drop. The For these reasons, the value of the pressure drop determined using knowledge from

the fundamental physics of the volcanic process is preferred for use in the model. However it is noted that this is the higher of the two estimations of the value of the pressure drop. For the range of parameter values stated above, the theoretical stress field around the cylinder is calculated and compared to the observations.

## RESULTS OF THE MOUNT ST HELENS MODEL

### Orientation of the stress field.

For models with cylinder radius 1 km and 0.75 km the orientation of the theoretical stress field around a cylindrical hole in an infinite elastic region is similar to the radial pattern of the stress field orientation inferred from the focal mechanism solutions. This basic agreement of observation and model illustrates the feasibility of the deflating cylinder hypothesis to explain the perturbation in the stress field at Mount St. Helens. The model with a cylinder of 0.5 km radius does not predict a stress field with a strongly circular orientation; the effect of the pressure drop does not dominate the stress field. This model is rejected as a model for the magma reservoir at Mount St. Helens and is not discussed further. Figures 4.1, 4.2 , 4.3 illustrate the orientation of the $\sigma_1$ and $\sigma_3$ axes and the magnitude of the deviatoric stress field evaluated at a distance 2 km from the center of the cylinders 1.0 km 0.75 km and 0.5 km in radius.

### Magnitude of the stress field

The magnitude of the stress field around the cylinder varies with the choices made for the model parameters. For Mount St. Helens, the distance at which the deviatoric stress field changes from a larger to a smaller value than the breaking stress of the rock is indicated by the abrupt cessation of seismicity, approximately 2 km from a

**Figure 4.1** Orientation of the maximum ($\sigma_1$) and minimum ($\sigma_3$) stresses and magnitude of the deviatoric stress ($\sigma_1$-$\sigma_3$) evaluated 2 km from a hole in an infinite region. The radius of the hole is 1 km. The boundary stresses ($P_1$ and $P_3$) represent estimates of the regional stress field at Mount St. Helens and pressures within the hole (P) represent estimates of the pressure within the magmatic reservoir after the May 18, 1980 eruption. The orientation of the stress field in (a), (b), and (c) show patterns similar to the observed stress field. The maximum value of $\sigma_1$-$\sigma_3$ increases as the value of $P_1$- $P_2$ increases, all values could induce earthquakes. (b) is the preferred model for Mount St. Helens. The orientation of North at Mount St. Helens is denoted by N.

Orientation of $\sigma_1$

Orientation of $\sigma_3$

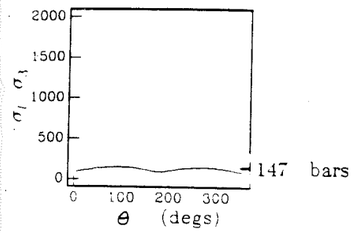


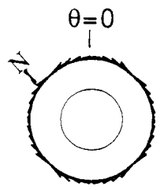


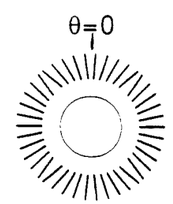


$P_1 = 2720$ bars $P_3 = 2680$ bars P = 2460 bars

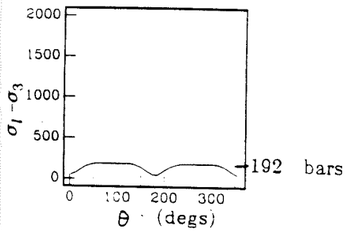


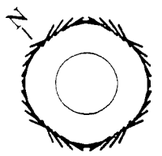


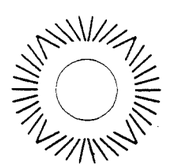

$P_1 = 2750$ bars $P_3 = 2650$ bars P = 2460 bars

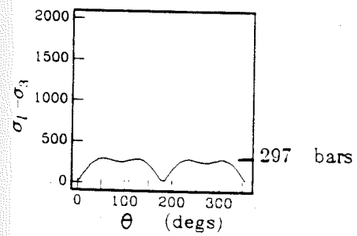


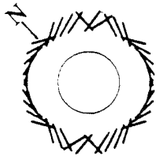


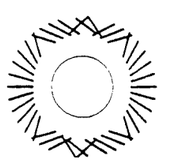

$P_1 = 2800$ bars $P_3 = 2600$ bars P = 2460 bars

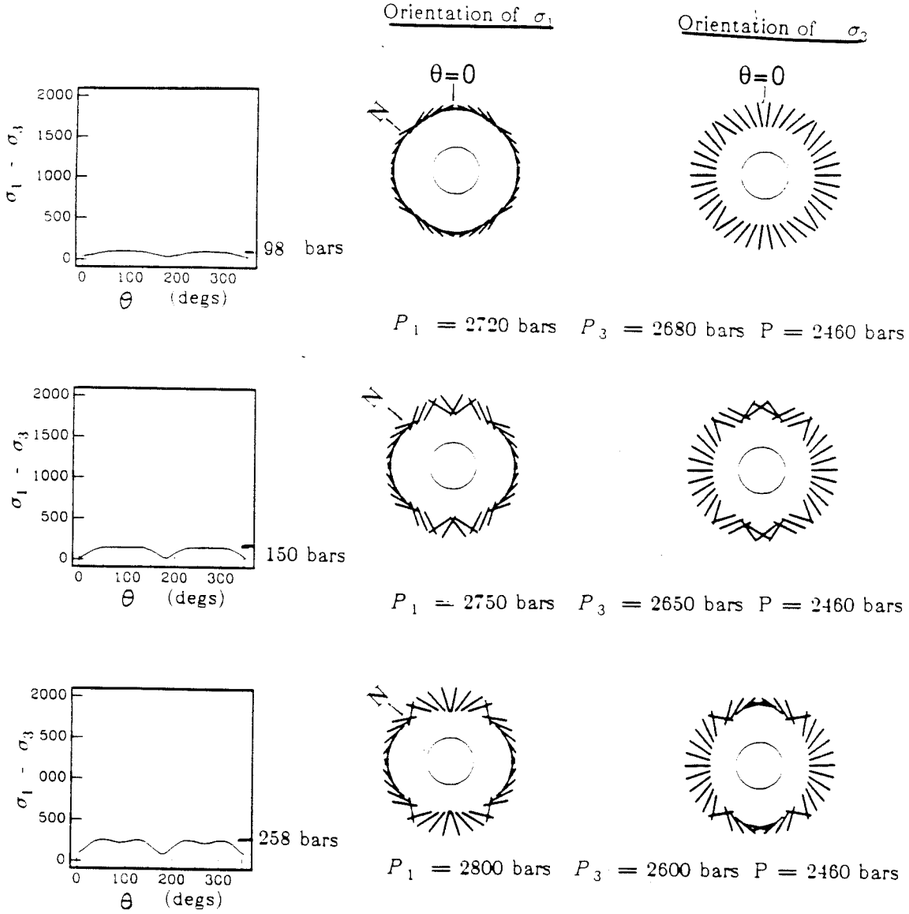


**Figure 4.2** Orientation of the maximum ($\sigma_1$) and minimum ($\sigma_3$) stresses and magnitude of the deviatoric stress ($\sigma_1$-$\sigma_3$) evaluated at 2 km from a hole in an infinite region. The radius of the hole is 0.75 km. Values of $P_1$, $P_3$, and P are the same as in figure 4.1. The theoretical stress field shows some resemblance of the stress field at Mount St. Helens, but the orientation is not predicated as well as by the model with a radius of 1 km. The orientation of North at Mount St. Helens is denoted by N.

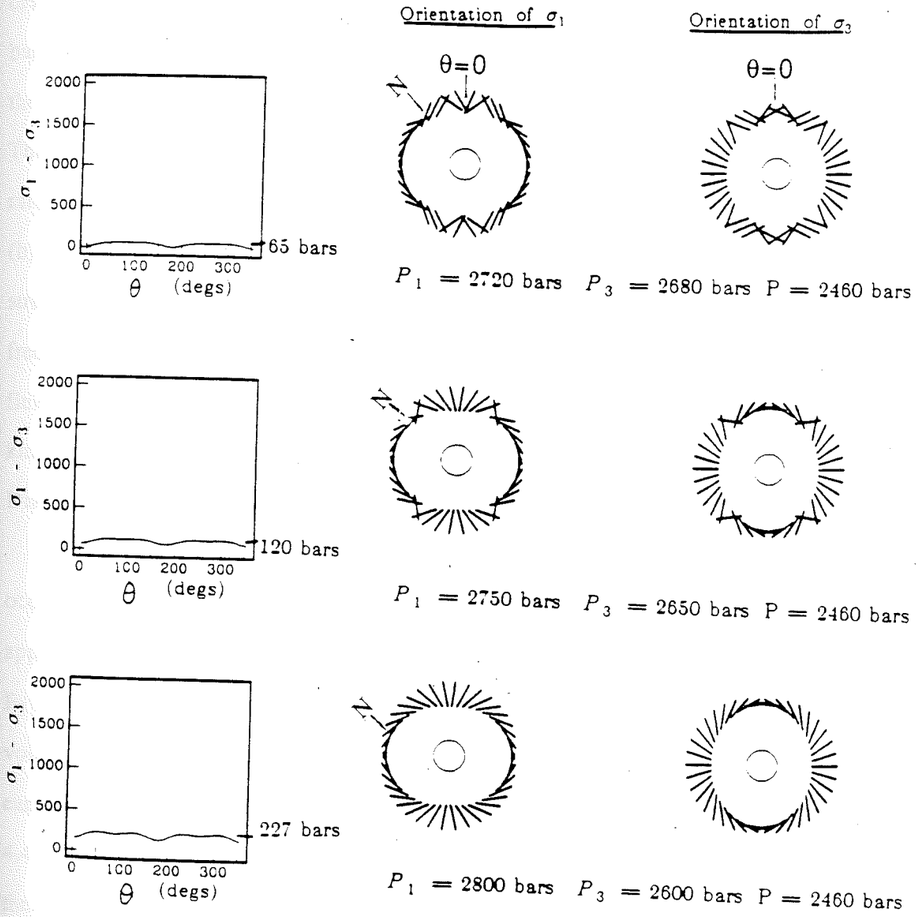


**Figure 4.3** Orientation of the maximum ($\sigma_1$) and minimum ($\sigma_3$) stresses and magnitude of the deviatoric stress ($\sigma_1$-$\sigma_3$) evaluated at 2 km from a hole in an infinite region. The radius of the hole is 0.5 km. Values of $P_1$, $P_3$, and P are the same as in figure 4.1. The circular nature of the stress field is not predicted as well as by the larger radii holes. This stress field shows characteristics of a shear stress field.

central point of the cylinder. The maximum values of the deviatoric stress ($\sigma_1$ - $\sigma_3$) at this distance for models with cylinders of radii 1.0 km and 0.75 km are between 147 and 297 bars. Assuming that the earthquakes relieve all the stress within the rock, the magnitude of the deviatoric stress is the maximum stress drop of an earthquake. Values measured by Thatcher and Hanks [1973] for stress drops of crustal earthquakes in Southern California range from 0.2 to 200 bars. For cylinders of radius 1 km and 0.75 km, models (a) and (b), the magnitude of the deviatoric stress field falls within this range . Actual earthquake stress drops cannot be easily estimated for the Mount St. Helens data due to the inadequate frequency range of the instrumentation and low Q, but both models have deviatoric stress fields which can produce earthquakes with stress drops in the range 0.2 to 200 bars at 2 km from the center of the cylinder.

**Distribution of seismicity**

If homogeneity of the rocks could be assumed one would expect most seismicity to occur where the deviatoric stress is largest, at azimuths parallel to the direction of the applied boundary minimum compressive stress ($P_3$). At Mount St. Helens the direction of $P_3$ is N60W, but the concentrations of seismicity are to the east and west of the aseismic volume and possibly the magma chamber. Comparison of the azimuthal distribution of earthquakes and the direction predicted by the deviatoric stress field are illustrated in fig 4.4. If one assumes that the deviatoric stress field is larger where earthquakes occur, then the distribution of earthquakes cannot satisfactorily be explained in terms of the magnitude of the deviatoric stress field for any of the models tested. The assumption that the rock in which the earthquakes occur is both homogeneous and of equal strength everywhere is probably not applicable. In a more realistic model, the location of seismicity would also be controlled by the effect of pre-existing weaknesses in the rock and not solely by the magnitude of the deviatoric stress field.

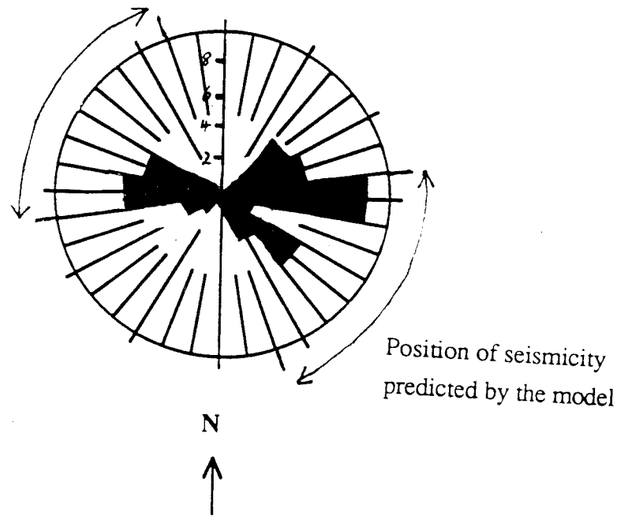


**Figure 4.4** Azimuthal distribution of post-eruptive earthquakes epicenters around the postition of the present day vent. Preferred direction for earthquakes distribution based on the model is indicated.

Although no surface faults that are associated with seismicity have been mapped in the region around Mount St. Helens, earthquakes appear to occur on fault segments lying in a north-south direction [Grant et al., 1984]. If weaknesses of this nature exist within the body of rock under the cone of Mount St. Helens, the most favorable stress regime for a series of faults oriented approximately north-south, exists to the east and west of the cylinder. If slip occurs on short discontinuous fault segments, the locations of the earthquakes and the inferred stress field orientation can be explained by the pressure drop within a cylinder.

From all the models tested the parameter values of 1 km radius and boundary stresses of 2750 and 2650 bars produce the closest representation of the stress field at Mount St. Helens. This model shows similar axes orientation as observed from the focal mechanism solutions and the magnitude of the deviatoric stress field predicted falls within the commonly accepted range of values for earthquake stress drop. The preference of the cylinder of 1 km radius over a model with a radius of 0.75 km suggests that the thickness of a plastic zone between the fluid part of the magma body and the competent rock in which the post-eruptive earthquakes occur is less than 0.25 km. I estimate that the radius of the magma body is approximately 0.9 km. Although the model suggested here is only a simple approximation of a magma body geometry which in reality is probably very complex, the preferred values for the model parameters provide an indication of the average parameter values. In addition the model illustrates the feasibility of a pressure drop within a magma body inducing earthquakes in the surrounding country rock.

# CHAPTER V

# DISCUSSION

## THE VOLCANIC SYSTEM AT MOUNT ST HELENS

Modeling of the stress field associated with the post-eruptive earthquakes located between the depths of 7 and 11 km, produces results that support the hypothesis proposed by Scandone and Malone [1985], and Shemeta and Weaver [1986] in which the post-eruptive earthquakes occur in response to a perturbation in the regional stress field, this change, in turn caused by a pressure decrease in a magmatic reservoir located between the seismic lobes. The post-eruptive earthquake swarm represents the rapid brittle readjustment of the volcanic system to the withdrawal of magma in the 12 hours immediately following the eruption [Scandone et al., 1985]. Aseismic adjustment followed the brittle failure and continued for a much longer time span than the post-eruptive swarm. In the months between May and November 1980, the Mount St. Helens volcano experienced a net subsidence of 20-70 cm [Swanson et al.,1981]. The style of readjustment may have occurred as suggested by Shaw [1980] analogous to his model for Hawaii, in which the upward flow of magma during a volcanic eruption is equilibrated by the downward displacement of the surrounding rocks.

Scandone et al. [1985] used geodetic data to estimate a 7 km depth for the Mount St. Helens reservoir. They assumed that the net subsidence of the volcanic edifice was related to the volume of magma equal to the cumulative volume of products erupted between May and October 1980. Petrologic studies by Rutherford et al. [1985] also indicate that glass inclusions within plagioclase phenocrysts in the extruded magma were formed at a depth of approximately 7 km . This depth defines the upper limit of the

position of the magma body estimated from hypocenter locations, and again illustrates the feasibility of the model.

The model that I have derived for the magmatic system at Mount St. Helens for depths between 6 and 20 km is illustrated is figure 5.1. From the modeling of the anomalous stress field of the upper part of the system a magma body of approximately 0.9 km radius is preferred, thus allowing for a zone of plastic deformation to occur before the onset of the seismicity and for brittle failure of the rocks to occur at a radial distance of 1.0 km. Because the east and west seismic lobes only extend to a depth of 11 km, this is interpreted to be the maximum depth of the magma body. The model does not predict the locations of the seismicity exactly, but it is possible that properties of the rock rather than the magnitude of the deviatoric stress controls the location of the earthquakes. I model the earthquakes that delineate the aseismic volume to occur on short discontinuous fault segments that are roughly tangential to the boundaries of the magma body. Located to the east and west of the present day vent they are in a position that is more preferentially aligned with a north south inherent weakness in the rock than if they occurred to the north and south.

The anomalous stress field does not extend below 11 km where the character of seismicity changes. These deeper events have larger magnitudes than the shallower seismicity and the focal mechanism solutions are similar to those of earthquakes which fall on the St. Helens seismic zone. I suggest that the post-eruptive seismicity between the depths of 12 and 20 km occurs on pre-existing faults in the rock that are preferentially aligned with respect to the regional stress field and may be an extension of the St. Helens seismic zone under the mountain. It is these pre-existing fractures that may open and allow transport of magma to the shallow volcanic system from a reservoir deeper in the crust. This magma flow may trigger the earthquakes on the fault system.

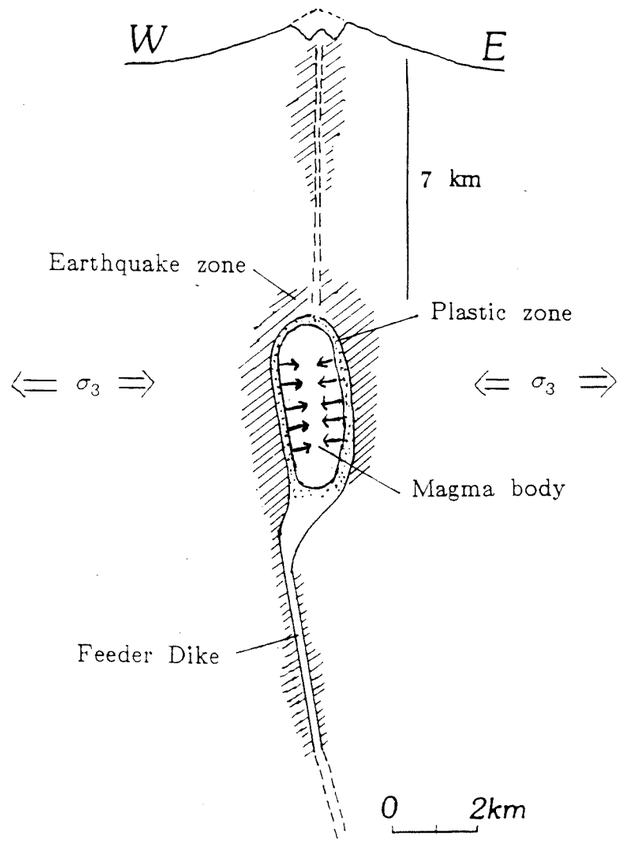


**Figure 5.1** A model for the geometry of the magmatic system at Mount St. Helens.

The volume of rock inferred to delineate the magma chamber is estimated to be on the order of 4 $km^3$. If seismic waves travel through magma, anomalous attenuation of the shear wave and a reduction in frequency of both the P and S waves occurs, as seen in the Long valley Caldera [ Ryall and Ryall, 1981]. For the rays studied in the determination of focal mechanism solutions at Mount St. Helens, the few whose paths apparently crossed the aseismic region did not experience a detectable change in P and S wave frequency, as seen at the Long Valley Caldera. This lack of attenuation is somewhat strange, but for the size of magma body suggested the number of rays that actually pass through the magma body may be very small. My search was not extensive and I would expect a more detailed study to be more successful in finding attenuated rays.

## CONCLUSIONS

The location of post-eruptive earthquakes following the explosive eruption of Mount St. Helens on 18 May, 1980 and 12 June, 1980 delineate an aseismic region which is the suggested location of a magma body [Scandone and Malone, 1985; Shemeta and Weaver, 1987]. The occurrence of an anomalous stress field in the depth range of 7-11 km directly beneath the volcanic edifice is inferred from this study of focal mechanism solutions. The source of this anomalous field can be successfully modeled as a cylinder undergoing a pressure decrease that is located within an elastic region, the boundaries of which experience stresses equivalent to the regional stress field at Mount St. Helens. The aseismic region is interpreted to be the location of a elongated magma body, which extends from a depth of 7 to 11 km, has a of radius 0.9 km and an estimated volume of 10 $km^3$.

## BIBLIOGRAPHY


Aki, K. (1980). Attenuation of shear waves in the lithosphere for frequencies from 0.05 to 25 Hz, *Physics of the Earth and Planetary Interiors*, **21**, 50-60.

Aki K., and P. G. Richards (1980). *Quantitative Seismology*, W. H. Freeman and Company, San Francisco, CA.

Christiansen, R. L. and D. W. Peterson. (1981). Chronology of the 1980 eruptive activity, U.S.*Geol. Surv. Prof. Pap.*, 1250, 17-30.

Davies, P. M., L. M. Hastie, and F. D. Stacey (1974). Stress within an active volcano - with particular reference to kilauea, *Tectonophysics*, **22**, 355-362.

Endo, E. T., S. D. Malone, L. L. Noson and C. S. Weaver (1981). Locations, magnitudes and statistics of the March 20 - May 18 earthquakes sequence. *U.S. Geol. Surv. Prof. Pap.*, 1250, 93-107.

Grant, W. C., and C. S. Weaver (1986). Earthquakes near Swift reservoir, Washington, 1958-1963: Seismicity along the southern St. Helens Seismic zone, *Bull. Seism. Soc. Am.* **76**,1573-1587.

Grant, W. C., C. S. Weaver, J. E. Zollweg (1984). The 14 February 1981 Elk Lake, Washington earthquake sequence, *Bull. Seism. Soc. Am.* **74**, 1289-1309.

Gutenburg, B., (1944). Energy ratio of reflected and refracted seismic waves, *Bull. Seism. Soc. Am.* **34**, 85-101.

Havskov, J., S. D. Malone, D. C. McClurg and R. S. Crosson (1988). Coda-Q of the State of Washington, submitted to *Bull. Seism. Soc. Am.*

Jaeger, J. C., (1969). *Elasticity, fracture and flow*, edited by B. L.Worsnop and G. K. T. Conn, Methuen & Co Ltd and Science Paperbacks, 187-188.

Kisslinger, C., (1980). Evaluation of S to P amplitude ratios for determining focal mechanisms from regional network observations, *Bull. Seism. Soc. Am.* **70**, 999-1014.

Kisslinger, C., J. R. Bowman, and K. Koch (1981). Procedures for computing focal mechanisms from local $(Sv/P)_z$ data, *Bull. Seism. Soc. Am.* **71**, 1719-1729.

Kisslinger, C. J. R. Bowman, and K. Koch (1982). Determination of focal mechanisms from Sv/P amplitude ratios at small distances, *Physics of the Earth and Planetary Interiors*, **30**, 172-176.

Lees, J. M. , and R. S. Crosson (1988). Tomographic inversion for 3-D velocity structure at Mount St. Helens using earthquakes data. Submitted to JGR. June 1988

Malone, S. D., C. Boyko, C. S. Weaver (1983). Seismic precursors to the Mount St. Helens eruptions in 1981 and 1982, *Science*, Vol. **221**, No. 4618, 1376-1387.

Malone, S. D., E. T. Endo, C.S. Weaver and J. W. Ramey (1981). Seismic monitoring for eruption prediction, *U.S. Geol. Surv. Prof. Pap.*, 1250, 808-813.

Malone, S. D. and G. L. Pavlis (1983). Velocity structure and relocation of earthquakes at Mount St. Helens (abstract). *American Geophysical Union, EOS Transactions*, No. **64**, 895.

McClurg, D.C. (1987). Coda-Q analysis at Mount St. Helens and its implications for volcanic seismology, Master's thesis, University of Washington.

Olhoeft, G. R., R. L. Reynolds, J. D. Friedman, G. R. Johnson, and G. R. Hunt, (1981). Physical properties of the June dacite dome, *U.S. Geol. Surv. Prof. Pap.*, 1250, 549-556.

Oppenheimer, D. H. (1986). Extensional tectonics at the geysers geothermal area , California,*J.Geophs. Res.*, **91**, 11,463-11,476.

Reasenberg, P., and D. Oppenheimer (1985). FPFIT, FPPLOT, and FPPAGE: Fortran computer programs for calculating and displaying earthquake fault-plane solutions, *U. S. Geol. Surv. Open File Rep.*, 109, 85-739 .

Rutherford, M.J., H. Sigudrsson, S. Carey, and A. Davis (1985). The May 18, 1980, eruption of Mount St. Helens: 1. Melt composition and experimental phase equilibria, *J. Geophs. Res.*, **90**, 2929-2947.

Ryall, F., A. Ryall (1981). Attenuation of P and S waves in a magma chamber in Long Valley caldera, California, *Geophs. Res.. Let*, **81**, 557-560.

Sarna-Wojcicki, A. M., C. E. Meyer, M.J.Woodard, and P. J. Lamothe (1981). Composition of air-fall ash erupted on May 18, May 25 , June12, July 22 and August 7, *U.S. Geol. Surv. Prof. Pap.*, 1250, 667-681.

Scandone, R., and S. D. Malone (1985). Magma supply, magma discharge and readjustment of the feeding system of Mount St. Helens during 1980, *J. Volcanol. Geotherm.* Res., **23**,239-262.

Shaw, H. R., (1980). The fracture mechanism of magma transport from the mantle to the surface, in: *Physics of magmatic processes.*, edited by R. B. Hargraves, Princeton Univ. Press, Princeton, N. Y., 201-264.

Shemeta, J.E., and C. S. Weaver (1986). Seismicity accompanying the May 18, 1980 eruption of Mount St. Helens, Washington, in *Mount St Helens: Five Years Later*, edited by S. A. C. Keller, Eastern Washington University Press, Chency 44-58.

Snoke, J. A., J. W. Munsey, A. G. Teague, and G. A. Bollinger (1984). A program for focal mechanisms determination by combined use of polarity and $S_V$-P amplitude ratio data, (abstract) *Earthquake Notes*, **55,** No. 3, 15.

Swanson, D. A., P. W. Lipman, J. G. Moore, C. C. Heliker, and K. M. Yamashita (1981). Geodetic monitoring after the May 18 eruption. *U.S. Geol. Surv. Prof. Pap.*, 1250,157-168.

Thatcher, W., and T. C. Hanks (1973). Source parameters of southern California earthquakes, *J. Geophs. Res.*, **78**, 35, 8547-8576.

Vvendenskaya, A. V., (1956). Determination of the displacement field of earthquakes by the use of dislocation theory (in Russian), *Izvest. Akad S.S.S.R., Ser, Geofiz.*, 3, 277-284.

Weaver, C. S., W. C. Grant, S. D. Malone, and E. T. Endo (1981). Post-May seismicity: Volcanic and tectonic implications, *U.S. Geol. Surv. Prof. Pap.*, 1250, 109-122

Weaver, C. S., and S. W. Smith (1983). Regional tectonic and earthquakes hazard implication of a crustal fault zone in southwestern Washington, *J. Geophs. Res.*, **88**. 10,371 - 10,383.

Weaver, C. S., W. C. Grant, J. E. Shemeta (1987). Local crustal extension at Mount St. Helens, Washington, *J. Geophs. Res.*, **92**, 10,170-10,178.

Williams, D. L., G. Adams, C. Finn, D. Dzursin, D. J. Johnson, R. Denlinger (1987). Evidence from gravity data for an intrusive complex beneath Mount St. Helens, *J. Geophs. Res.*, **92**, 10,210-10,222.

## APPENDIX A: Focal Mechanism Solutions of Post-eruptive Earthquakes

**Table A.1** Post-eruptive Earthquake Data
Locations and mean focal mechanism solutions

| ID | Date | Time | °N Latitude | °W Longitude | Depth | M | P axis Strike | P axis Dip | T axis Strike | T axis Dip |
|---|---|---|---|---|---|---|---|---|---|---|
| 1 | May 19, 1980 | 0021 | 46.1364 | 122.1150 | 17.39 | 2.1 | 127 | 37 | 346 | 46 |
| 2 | May 19, 1980 | 0051 | 46.1224 | 122.1261 | 12.55 | 3.5 | 139 | 3 | 240 | 74 |
| 3 | May 19, 1980 | 0052 | 46.1287 | 122.1244 | 15.48 | 3.5 | 170 | 48 | 262 | 2 |
| 4 | May 19, 1980 | 0055 | 46.1356 | 122.1159 | 17.09 | 2.8 | 68 | 38 | 302 | 38 |
| 5 | May 19, 1980 | 0057 | 46.1280 | 122.1206 | 14.04 | 3.9 | 22 | 27 | 128 | 27 |
| 6 | May 19, 1980 | 0106 | 46.1185 | 122.1211 | 17.43 | 2.2 | 175 | 16 | 269 | 14 |
| 7 | May 19, 1980 | 0111 | 46.1332 | 122.1167 | 18.30 | 3.6 | 151 | 62 | 284 | 20 |
| 8 | May 19, 1980 | 0121 | 46.1285 | 122.1117 | 17.72 | 3.3 | 77 | 1 | 346 | 38 |
| 9 | May 19, 1980 | 0126 | 46.1262 | 122.1262 | 7.80 | 1.7 | 253 | 54 | 94 | 34 |
| 10 | May 19, 1980 | 0129 | 46.1309 | 122.1150 | 19.36 | 2.6 | 33 | 5 | 126 | 31 |
| 11 | May 19, 1980 | 0136 | 46.1231 | 122.1006 | 7.57 | 2.6 | 161 | 27 | 300 | 56 |
| 12 | May 19, 1980 | 0200 | 46.1286 | 122.1175 | 14.44 | 1.7 | 198 | 12 | 341 | 75 |
| 13 | May 19, 1980 | 0209 | 46.1297 | 122.1126 | 19.49 | 2.3 | 5 | 4 | 95 | 4 |
| 14 | May 19, 1980 | 0217 | 46.1332 | 122.1108 | 18.01 | 1.7 | 236 | 14 | 81 | 75 |
| 15 | May 19, 1980 | 0258 | 46.1337 | 122.1146 | 17.61 | 1.9 | 246 | 46 | 27 | 37 |
| 16 | May 19, 1980 | 0311 | 46.1326 | 122.1154 | 18.77 | 1.9 | 44 | 20 | 153 | 42 |
| 17 | May 19, 1980 | 0350 | 46.1335 | 122.1154 | 17.50 | 1.2 | 238 | 27 | 133 | 27 |
| 18 | May 19, 1980 | 0436 | 46.1260 | 122.1243 | 12.47 | 2.5 | 176 | 5 | 78 | 57 |
| 19 | May 19, 1980 | 0443 | 46.1191 | 122.0982 | 11.37 | 1.8 | 323 | 19 | 78 | 51 |
| 20 | May 19, 1980 | 0528 | 46.1195 | 122.0979 | 10.63 | 2.0 | 236 | 26 | 142 | 8 |
| 21 | May 19, 1980 | 0545 | 46.1304 | 122.1224 | 13.87 | 2.1 | 6 | 4 | 97 | 18 |
| 22 | May 19, 1980 | 0546 | 46.1185 | 122.0969 | 11.44 | 1.7 | 24 | 7 | 114 | 1 |
| 23 | May 19, 1980 | 0648 | 46.1221 | 122.1054 | 9.15 | 0.9 | 336 | 13 | 73 | 27 |
| 24 | May 19, 1980 | 0701 | 46.1203 | 122.1076 | 8.32 | 0.4 | 202 | 8 | 110 | 17 |
| 25 | May 19, 1980 | 0709 | 46.1205 | 122.1087 | 9.85 | 0.2 | 245 | 33 | 139 | 23 |
| 26 | May 19, 1980 | 0718 | 46.1263 | 122.1210 | 15.44 | 3.6 | 6 | 23 | 236 | 57 |
| 27 | May 19, 1980 | 0721 | 46.1372 | 122.1028 | 9.07 | 1.5 | 330 | 43 | 238 | 3 |
| 28 | May 19, 1980 | 0723 | 43.1254 | 122.1019 | 10.80 | 0.4 | 158 | 20 | 265 | 39 |
| 29 | May 19, 1980 | 0752 | 46.1204 | 122.1007 | 10.66 | 0.6 | 17 | 17 | 114 | 20 |
| 30 | May 19, 1980 | 0858 | 46.1180 | 122.1258 | 10.30 | 1.9 | 332 | 7 | 88 | 74 |
| 31 | May 19, 1980 | 0901 | 46.1269 | 122.1009 | 10.00 | 1.0 | 331 | 7 | 62 | 7 |
| 32 | May 19, 1980 | 0910 | 46.1205 | 122.1040 | 10.50 | 1.9 | 15 | 14 | 117 | 41 |
| 33 | May 19, 1980 | 1151 | 46.1215 | 122.1010 | 10.65 | 1.8 | 74 | 24 | 230 | 64 |
| 34 | May 19, 1980 | 1227 | 46.1220 | 122.1024 | 10.39 | 0.7 | 6 | 1 | 274 | 59 |

Table A.1 continued

| ID | Date | Time | °N Latitude | °W Longitude | Depth | M | P axis Strike | P axis Dip | T axis Strike | T axis Dip |
|---|---|---|---|---|---|---|---|---|---|---|
| 35 | May 19, 1980 | 1246 | 46.1149 | 122.1220 | 11.36 | 0.7 | 111 | 44 | 3 | 17 |
| 36 | May 19, 1980 | 1251 | 46.1243 | 122.1031 | 8.52 | 0.5 | 40 | 12 | 135 | 21 |
| 37 | May 19, 1980 | 1421 | 46.1297 | 122.1297 | 14.69 | 3.6 | 341 | 11 | 115 | 74 |
| 38 | May 19, 1980 | 1621 | 46.1174 | 122.1063 | 10.35 | 0.5 | 62 | 12 | 328 | 17 |
| 39 | May 19, 1980 | 1821 | 46.1282 | 122.1224 | 15.35 | 2.1 | 332 | 16 | 95 | 63 |
| 40 | June 13, 1980 | 0648 | 46.1227 | 122.1232 | 8.03 | 0.4 | 187 | 26 | 80 | 30 |
| 41 | June 13, 1980 | 0708 | 46.1197 | 122.1218 | 8.34 | 0.6 | 323 | 42 | 77 | 25 |
| 42 | June 13, 1980 | 0732 | 46.1209 | 122.1215 | 8.45 | 0.5 | 312 | 40 | 93 | 43 |
| 43 | June 13, 1980 | 0751 | 46.1211 | 122.1244 | 8.21 | 1.0 | 313 | 0 | 46 | 53 |
| 44 | June 13, 1980 | 0828 | 46.1211 | 122.1071 | 11.46 | 0.3 | 205 | 28 | 77 | 49 |
| 45 | June 13, 1980 | 0932 | 46.1154 | 122.1041 | 8.99 | 0.6 | 48 | 8 | 318 | 0 |
| 46 | June 13, 1980 | 0936 | 46.1215 | 122.1219 | 8.03 | 1.1 | 242 | 16 | 133 | 48 |
| 47 | June 13, 1980 | 1000 | 46.1203 | 122.1238 | 8.18 | 1.0 | 163 | 18 | 254 | 4 |
| 48 | June 13, 1980 | 1030 | 46.1240 | 122.1253 | 8.40 | 1.3 | 173 | 9 | 79 | 22 |
| 49 | June 13, 1980 | 1129 | 46.1203 | 122.1214 | 6.97 | 1.1 | 341 | 20 | 75 | 19 |
| 50 | June 13, 1980 | 1338 | 46.1219 | 122.1231 | 8.02 | 1.6 | 337 | 11 | 90 | 63 |

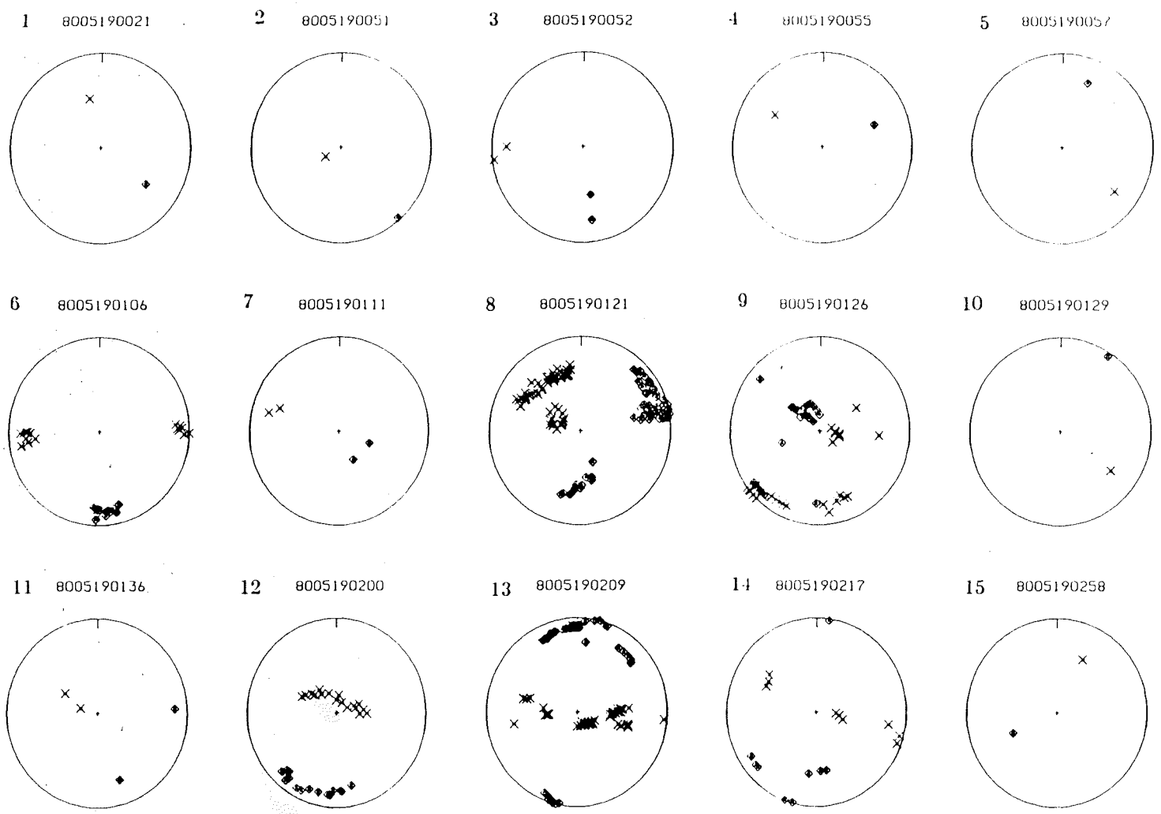


**Figure A.1** P (◊) and T (x) axes determined for the post-eruptive earthquakes. Where only 1 or 2 solutions are shown, they have been determined using fpfit.

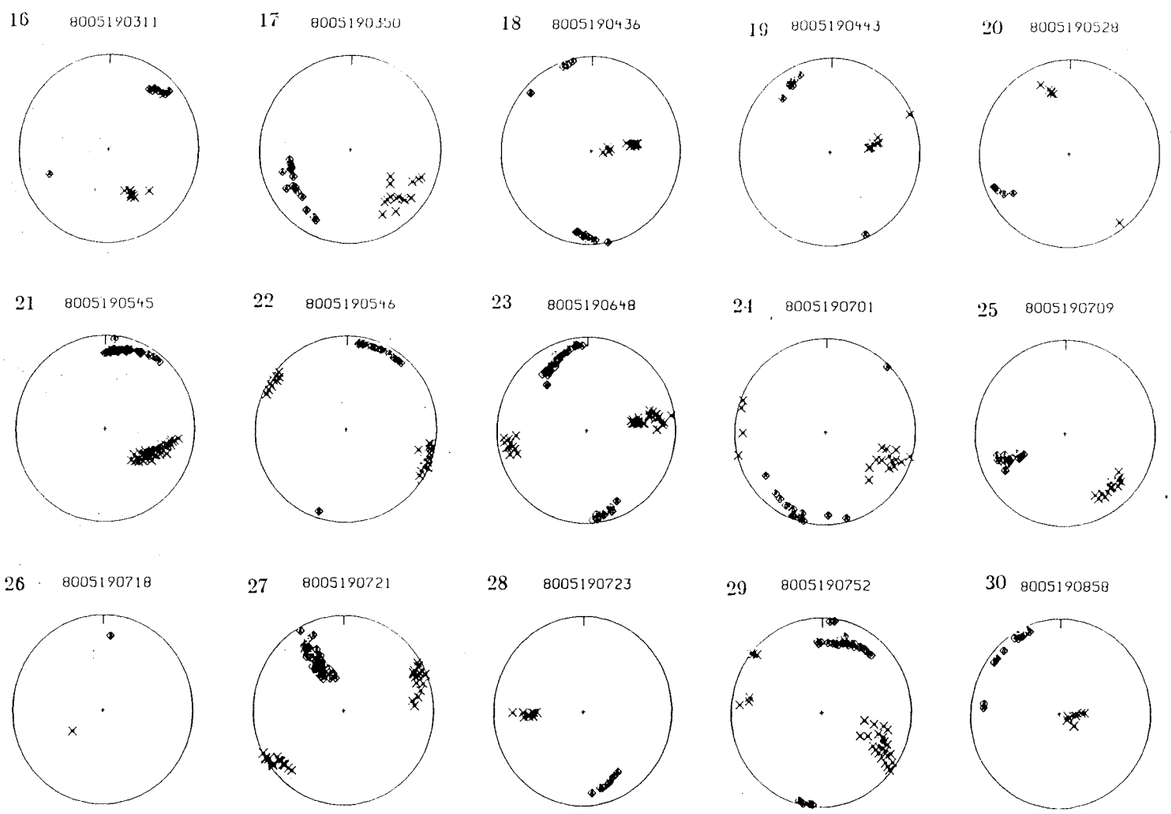


**Figure A.1** (continued)

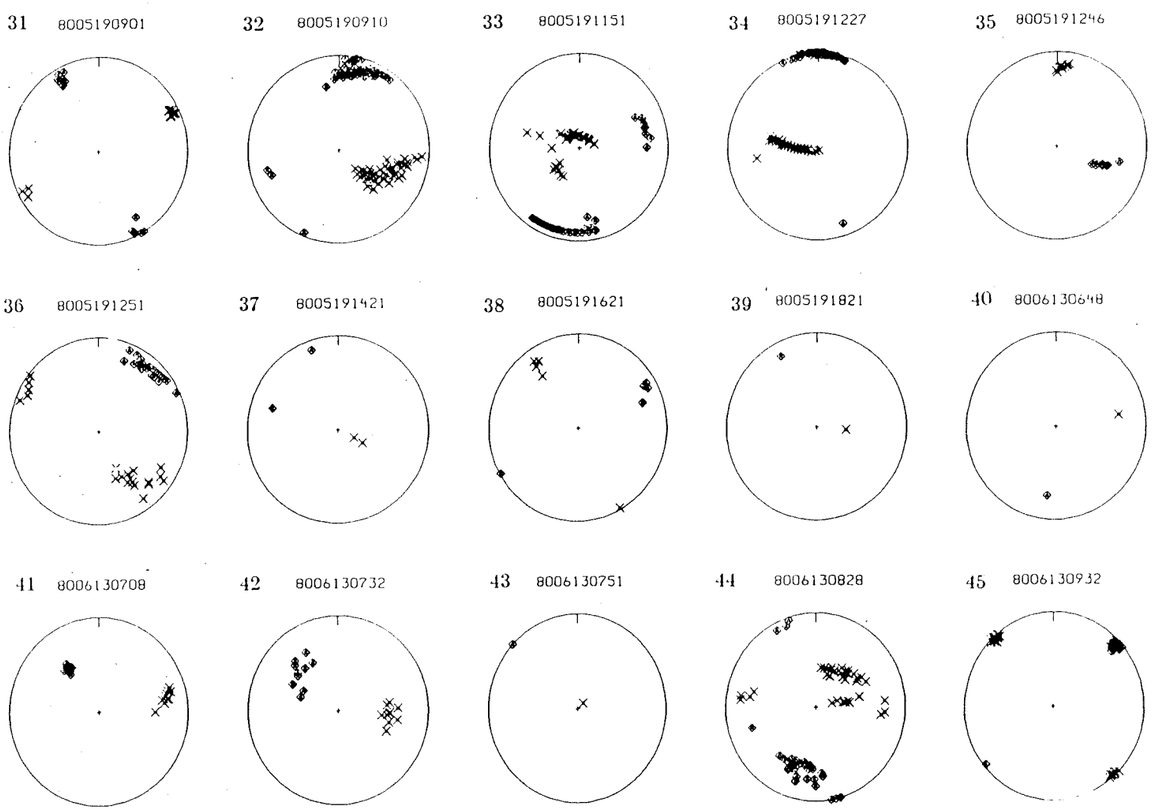


**Figure A.1** (continued)

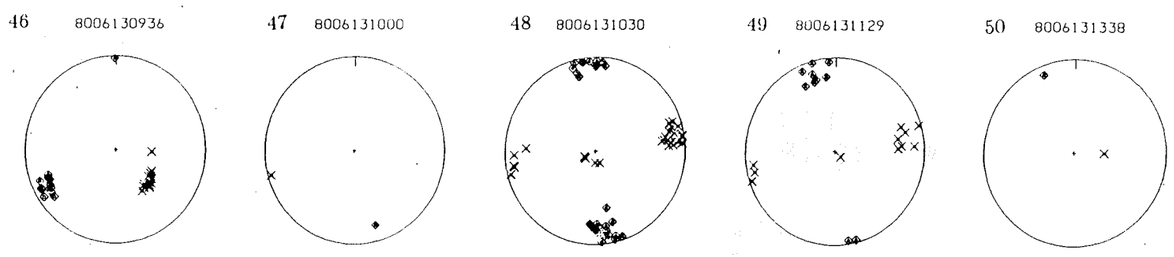


**Figure A.1** (continued)

## APPENDIX B: Focal Mechanism Solutions of Regional Earthquakes

**Table B.1** Regional Earthquake Data
Locations and mean focal mechanism solutions

| ID | Date | Time | °N Latitude | °W Longitude | Depth | M | P axis Strike | P axis Dip | T axis Strike | T axis Dip |
|---|---|---|---|---|---|---|---|---|---|---|
| 1 | March 26, 1980 | 0600 | 46.1083 | 122.0952 | 6.0 | 3.5 | 100 | 45 | 349 | 20 |
| 2 | May 21, 1980 | 1345 | 46.1016 | 122.0793 | 12.42 | 2.6 | 51 | 17 | 176 | 62 |
| 3 | May 22, 1980 | 2149 | 46.1613 | 122.1241 | 7.09 | 2.2 | 24 | 72 | 204 | 18 |
| 4 | June 2, 1980 | 0035 | 46.1241 | 122.0737 | 8.65 | 0.9 | 23 | 4 | 120 | 60 |
| 5 | June 12, 1980 | 0248 | 46.1565 | 122.1539 | 11.43 | 0.9 | 229 | 24 | 133 | 12 |
| 6 | June 13, 1980 | 0538 | 46.1505 | 122.1190 | 8.80 | 0.9 | 229 | 33 | 105 | 40 |
| 7 | June 16, 1980 | 1353 | 46.1745 | 122.1357 | 12.36 | 1.1 | 211 | 39 | 105 | 18 |
| 8 | June 22, 1980 | 0708 | 46.2143 | 122.1479 | 6.76 | 1.0 | 36 | 46 | 129 | 3 |
| 9 | June 25, 1980 | 1759 | 46.0620 | 122.0735 | 6.03 | 1.8 | 268 | 32 | 128 | 51 |
| 10 | June 27, 1980 | 1440 | 46.2218 | 122.1628 | 15.08 | 1.6 | 207 | 46 | 309 | 11 |
| 11 | June 27, 1980 | 2004 | 46.2018 | 122.1534 | 13.06 | 0.5 | 213 | 23 | 120 | 8 |
| 12 | June 27, 1980 | 2159 | 46.1740 | 122.2174 | 15.94 | 1.2 | 18 | 10 | 285 | 15 |
| 13 | July 7, 1980 | 1130 | 46.1795 | 122.1325 | 7.69 | 1.7 | 34 | 60 | 170 | 23 |
| 14 | July 20, 1980 | 1330 | 46.0603 | 122.0701 | 5.17 | 2.8 | 212 | 23 | 113 | 20 |
| 15 | July 20, 1980 | 1422 | 46.1027 | 122.0752 | 9.31 | 3.7 | 27 | 7 | 123 | 44 |
| 16 | July 20, 1980 | 1736 | 46.0621 | 122.0729 | 6.04 | 2.6 | 203 | 5 | 110 | 28 |
| 17 | July 23, 1980 | 1038 | 46.0569 | 122.0713 | 5.99 | 2.7 | 30 | 4 | 120 | 4 |
| 18 | Aug . 8, 1980 | 2104 | 46.0625 | 122.0548 | 12.11 | 2.0 | 245 | 13 | 150 | 19 |
| 19 | Aug 15, 1980 | 0029 | 46.1030 | 122.0722 | 9.06 | 1.9 | 193 | 14 | 306 | 58 |
| 20 | Sept.12, 1980 | 0749 | 46.1000 | 122.0932 | 7.75 | 1.3 | 40 | 8 | 134 | 28 |
| 21 | Nov.12, 1980 | 0130 | 46.1229 | 122.0958 | 7.07 | 0.4 | 23 | 1 | 293 | 8 |
| 22 | Nov.14, 1980 | 1907 | 46.1022 | 122.0681 | 8.43 | 1.1 | 154 | 16 | 259 | 43 |
| 23 | Nov.17, 1980 | 0658 | 46.2631 | 122.2291 | 10.62 | 2.1 | 204 | 1 | 113 | 33 |
| 24 | Feb . 7, 1981 | 1226 | 46.1430 | 122.0672 | 9.92 | 1.2 | 229 | 20 | 132 | 18 |
| 25 | April 21, 1981 | 0353 | 46.1038 | 122.1858 | 12.56 | 1.5 | 346 | 28 | 236 | 32 |
| 26 | June 2, 1981 | 0411 | 46.0365 | 122.2191 | 16.34 | 1.3 | 156 | 21 | 319 | 68 |
| 27 | June 28, 1981 | 2321 | 46.0283 | 122.2637 | 17.48 | 1.2 | 340 | 15 | 160 | 75 |
| 28 | July 4, 1981 | 1850 | 46.0536 | 122.0832 | 8.87 | 1.4 | 185 | 37 | 83 | 16 |
| 29 | Aug. 4, 1981 | 1628 | 46.1307 | 122.1845 | 8.99 | 1.1 | 37 | 9 | 272 | 75 |
| 30 | Sept. 3, 1982 | 0331 | 46.1431 | 122.0672 | 9.32 | 1.8 | 60 | 16 | 246 | 74 |
| 31 | May 17, 1983 | 1527 | 46.0960 | 122.2333 | 10.48 | 1.0 | 198 | 33 | 86 | 30 |
| 32 | Dec. 11, 1986 | 0510 | 46.1271 | 122.2574 | 7.98 | 1.7 | 102 | 12 | 299 | 77 |
| 33 | July 22, 1987 | 0102 | 46:1117 | 122.1977 | 10.91 | 1.2 | 195 | 3 | 286 | 23 |
| 34 | Aug. 29, 1987 | 0237 | 46.1300 | 122.2010 | 9.95 | 1.3 | 12 | 1 | 252 | 88 |

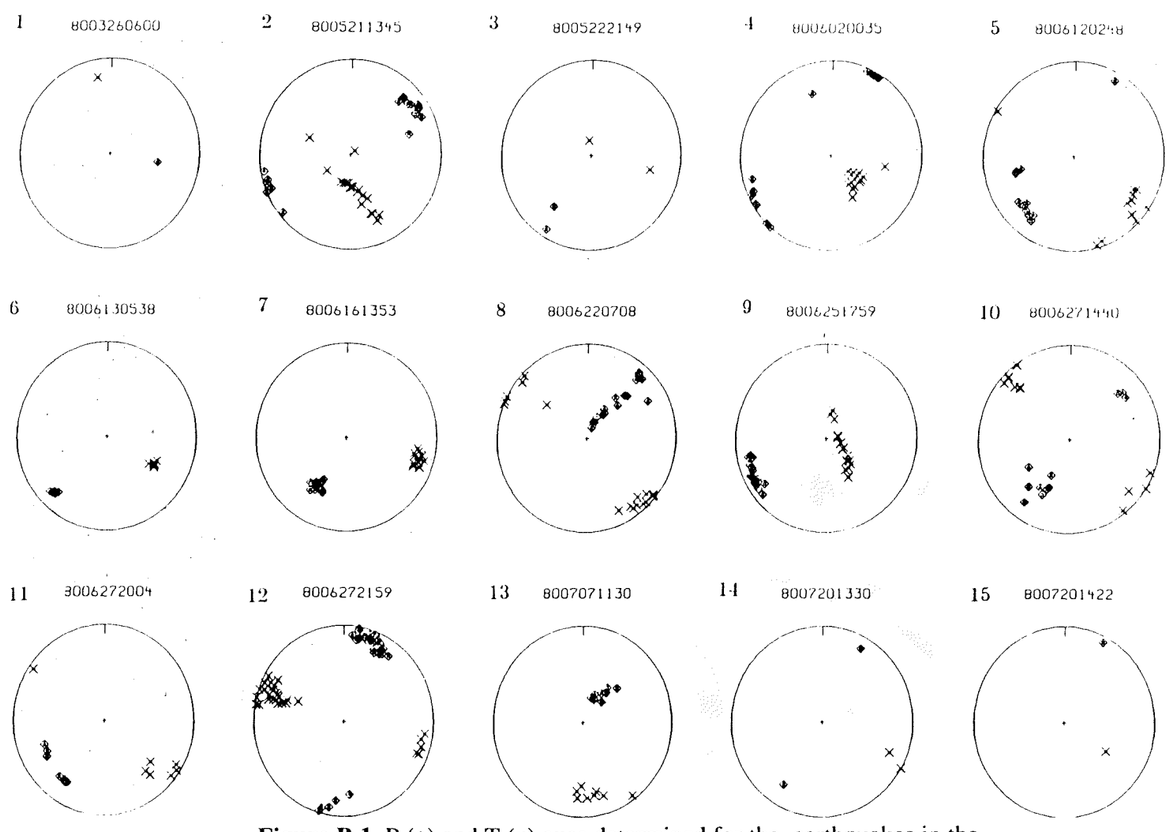


**Figure B.1** P (⊙) and T (x) axes determined for the earthquakes in the region around Mount St. Helens.Where only 1 or 2 solutions are shown, they have been determined using fpfit.

**Figure B.1** (continued)

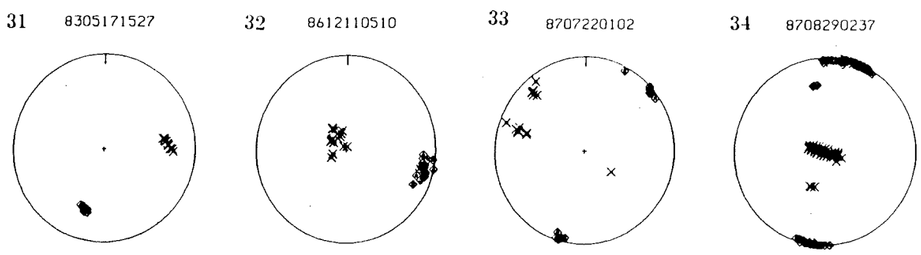


**Figure B.1** (continued)